



DEPARTMENT OF ELECTRICAL ENGINEERING
INDIAN INSTITUTE OF TECHNOLOGY MADRAS
CHENNAI – 600036

Analysis and Optimization of Fixed-Frequency Superconducting Quantum Processors

A Thesis

Submitted by

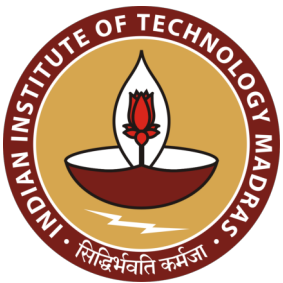
GAUTHAM UMASANKAR

For the award of the degree

Of

MASTER OF TECHNOLOGY, QUANTUM SCIENCE AND TECHNOLOGY

July 2022



DEPARTMENT OF ELECTRICAL ENGINEERING
INDIAN INSTITUTE OF TECHNOLOGY MADRAS
CHENNAI – 600036

Analysis and Optimization of Fixed-Frequency Superconducting Quantum Processors

A Thesis

Submitted by

GAUTHAM UMASANKAR

For the award of the degree

Of

MASTER OF TECHNOLOGY, QUANTUM SCIENCE AND TECHNOLOGY

July 2022

All equations speak, we just have to listen...

– Rakesh Reddy

*To my parents and grandparents, who taught me what it is to lead
a good life*

THESIS CERTIFICATE

This is to undertake that the Thesis titled **ANALYSIS AND OPTIMIZATION OF FIXED-FREQUENCY SUPERCONDUCTING QUANTUM PROCESSORS**, submitted by me to the Indian Institute of Technology Madras, for the award of **Master of Technology, Quantum Science and Technology**, is a bona fide record of the research work done by me under the supervision of **Dr. Rajamani Vijayaraghavan**. The contents of this Thesis, in full or in parts, have not been submitted to any other Institute or University for the award of any degree or diploma.

Chennai 600036

Date: July 2022



Gautham Umasankar



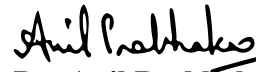
Dr. Rajamani Vijayaraghavan

Research advisor

Associate Professor

Department of Condensed Matter Physics and Material Science

Tata Institute of Fundamental Research



Dr. Anil Prabhakar

Research co-advisor

Professor

Department of Electrical Engineering

IIT Madras

ACKNOWLEDGEMENTS

"If I have seen further, it is by standing on the shoulders of giants". There are so many people who have been integral to the work done in this thesis. I would like to thank my guide Prof. Rajamani Vijayaraghavan, TIFR, who has been a constant source of guidance and support throughout this project. If not for his patience, mentoring and encouragement, this would not have been possible. I would like to thank Sumeru Hazra, for teaching me most of the fundamentals I know in the field of circuit quantum electrodynamics and for patiently answering all my questions. Sumeru has been an inspiring mentor both in the lab and outside it.

I would like to thank Prof. Anil Prabhakar and Prof. Prabha Mandayam for setting up the Quantum Science and Technology dual degree at IITM. For students interested in a niche field like myself, this was a big opportunity and gave me the time and space needed to explore and find my interests in this field as the first batch of this dual degree. Prof. Anil's guidance in my previous projects set me up to be a better researcher, and his support helped me set up my Master's thesis project.

I would like to thank Jay Deshmukh for all the discussions we had, and the various bugs we resolved together. His wit and friendship were a constant source of support throughout my project. Anirban's patient instruction is the reason I was able to learn and run finite element simulations, and I would like to thank him for that. I would also like to thank Dr. Madhavi Chand, Kishor, Srijita, Nicolas, and Gaurav; I would not have enjoyed my time at the QuMaC lab as much without them.

I would like to thank all my friends; Keshav, Madhav, Nishant, Bharati, Pooja, Siva, Saikrishna, Sahana, Sumanth, Parth, and Ishwarya. They kept me going in spite of ups and downs, and have given me invaluable support. I would also like to thank my family, whose constant love and encouragement have been an integral part of all my endeavours.

ABSTRACT

Superconducting circuits have emerged as a leading platform for the implementation and realization of quantum computing applications. Specifically, the transmon qubit has become one of the most commonly used qubits in today's quantum computers based on superconducting circuits. The most common two-qubit gate in such fixed-frequency architectures is the Cross Resonance gate. This gate imposes certain constraints on the device parameters of the qubits present in a network. We investigate the intrinsic fidelity of this gate and study methods to quantify various sources of error like imperfect rotation within the computational subspace and leakage outside the subspace.

We extend these methods to multi-qubit networks and to single qubit gates. These methods are employed to study a 7 qubit processor with a particular connectivity. Design choices like the frequencies of the qubits are validated using these methods, and tolerances on qubit frequencies are estimated. We also discuss finite element electromagnetic simulations to engineer this seven qubit processor where the qubits are coupled via a ring-resonator. We conclude the discussion with possible extensions of these methods and other diagnostic metrics we can apply to the processor.

CONTENTS

	Page
ACKNOWLEDGEMENTS	i
ABSTRACT	iii
LIST OF TABLES	vii
LIST OF FIGURES	ix
CHAPTER 1 SUPERCONDUCTING QUBITS - AN INTRODUCTION	1
1.1 The Transmon Qubit	2
1.1.1 Hamiltonian of a Single Transmon Qubit	4
1.2 Quantum Gates on Transmon Qubits	6
1.2.1 Single Qubit Gates: Rabi Oscillations	6
1.2.2 Coupled Transmon Qubits and Two Qubit Gates	8
1.3 Thesis Outline	9
CHAPTER 2 THE CROSS RESONANCE GATE	11
2.1 System Hamiltonian	11
2.2 Effective Hamiltonian Theory	13
2.3 Cross Resonance Gate Fidelity and Error Budget	16
2.3.1 Time Evolution: Extracting and Analysing the Unitary Propagator	17
2.3.2 Gate Time Calibration	19
2.3.3 Fidelity and Sources of Error	20
2.4 Extension to Multiple qubits	22
2.4.1 Constructing Relevant Families of Unitary Matrices	24
2.5 Multiple Qubits - Key Results and Comparison	26
CHAPTER 3 OPTIMIZING MULTI-QUBIT NETWORKS	29
3.1 Constraints and Coherent Errors in Connected Qubit Networks	29
3.1.1 Constraints Imposed by the Cross Resonance Gate	29
3.1.2 Static ZZ Error	30
3.2 Choosing Qubit Frequencies in the 7 Qubit Processor	31
3.2.1 Static ZZ Error in the 7 Qubit Processor	32
3.3 Error Budget Analysis of the 7 Qubit Processor	34
3.3.1 Gate Fidelity vs Spectator Frequency	34
3.3.2 Results on Cross Resonance Gates in Various Subsets	37
CHAPTER 4 QUBIT DESIGN IN A 7 QUBIT RING-RESONATOR BASED PROCESSOR	41
4.1 Qubit Capacitance	43

4.2	Readout Coupling	44
4.3	Inter Qubit Coupling	47
CHAPTER 5 CONCLUSIONS AND FUTURE WORK		51
5.1	Enhancing the Gate Set	51
5.2	Optimal Control Techniques	52
5.3	Processor Diagnostics: Effective Hamiltonian Estimation and Stability .	53
5.4	Mixed Integer Programming to Optimize Qubit Frequencies	54
5.5	Conclusion	55
APPENDIX A MATHEMATICAL METHODS		57
A.1	Methods: Estimating the Closest Unitary	57
A.1.1	Two Qubit Analysis	57
A.1.2	Multiqubit Computation	58
A.2	Computational Methods Used	60
REFERENCES		61

LIST OF TABLES

Table	Caption	Page
2.1	Two qubit resonances in a system with constant coupling	15
2.2	Resonances in a three qubit system with constant coupling	16

LIST OF FIGURES

Figure	Caption	Page
1.1	Energy levels of an LC Oscillator vs a transmon qubit	3
1.2	Driving and coupling transmon qubits	7
1.3	Single qubit gates with Rabi oscillations on a transmon qubit	8
2.1	Schematic representation of the cross resonance gate	12
2.2	A visualization of the CR gate on the Bloch sphere	13
2.3	Effective Hamiltonian terms of the CR gate vs control-target detuning .	14
2.4	A schematic of a CR gate with a spectator qubit coupled to the control .	15
2.5	Pulse amplitude as a function of time for the modelling of the CR gate .	18
2.6	Calibration of the CR gate	20
2.7	Gate error vs drive strength for the CR gate	21
2.8	Error budget as a function of drive strength for the CR gate	23
2.9	CR gate calibration for two qubits and three qubits	27
2.10	Gate error vs drive strength for two qubits and three qubits	27
2.11	Error budget of the CR gate for a three qubit system	28
3.1	Schematic of the static ZZ error between coupled transmons	30
3.2	Connectivity in the seven qubit processor	32
3.3	Candidate frequency choices for the seven qubit processor	32
3.4	Static ZZ shifts in the seven qubit processor	33
3.5	Gate error vs control-spectator detuning; tolerance in frequency drift .	36
3.6	Change in gate error with system size	38
3.7	Change in single qubit gate error with system size	39
4.1	Double ring-resonator architecture for the seven qubit processor	42
4.2	Qubit capacitance computed with electrostatic simulation	44
4.3	Estimating cavity-qubit coupling	46
4.4	Estimating qubit-qubit coupling	48
5.1	Other CR based gates and optimal control	52
5.2	Mixed integer programming for qubit frequency allocation	55

CHAPTER 1

SUPERCONDUCTING QUBITS - AN INTRODUCTION

Quantum computers promise to revolutionize many computing applications. This computational power arises from the fundamental difference between quantum computers and classical computers. Quantum computers use "quantum bits" or "qubits" as their building blocks, as opposed to classical bits, which take only values 0,1. Qubits are 2-dimensional complex Hilbert spaces. Their state is described by a vector of the form:

$$|\psi\rangle = a|0\rangle + b|1\rangle \quad (1.1)$$

This allows qubits to be in arbitrary superposition states and greatly increases the size of the spaces we can explore simultaneously. Qubits can also be entangled, which causes their states to be highly correlated. Superposition allows us to explore exponentially larger Hilbert spaces as the number of qubits increases. For example, 2 qubits gives us a 4-D Hilbert space spanned by $|00\rangle, |01\rangle, |10\rangle, |11\rangle$, 3 qubits gives us an 8-D Hilbert space, and so on.

All these features make quantum computers superior to classical computers in certain operations like factoring large numbers (Shor's Algorithm - Shor (1997)), database searching (Grover's Algorithm - Grover (1996)). Since atoms and molecules behave quantum mechanically, quantum computers are also ideally suited for simulating quantum systems like strongly interacting Fermions. (Brown *et al.* (2010)).

However, the task of building and scaling quantum computers is no mean feat. There are various engineering challenges that need to be overcome. Quantum states are fragile because qubits interact with the environment, and such noise corrupts quantum information at much smaller timescales than classical bits. This effect is called

decoherence. Practically useful computation is possible only if we can perform our operations and measurements faster than this decoherence timescale. There are various other criteria that need to be met to create a scalable hardware platform for quantum computing, which are neatly described by DiVincenzo's criteria (DiVincenzo (2000)).

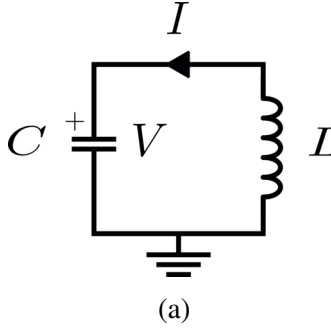
Some of the most promising platforms for building quantum computers are superconducting circuits (Devoret and Martinis (2004)), ion traps (Munro *et al.* (2000)), quantum dots (Loss and DiVincenzo (1998)), Nitrogen Vacancy Centers in Diamond (Childress and Hanson (2013)), etc.

Superconducting circuits are one of the most prominent approaches and use nanofabricated integrated circuits to create qubits. Superconductivity allows macroscopic variables like current and voltage to behave quantum mechanically. Besides this, the low dissipation in such circuits also reduces decoherence. The flexibility in nanofabrication techniques and circuit design also allows a high degree of control on the Hamiltonian that we build. Controlling such circuits is also feasible using easily available microwave hardware. With this in mind, we shall explore the creation of a superconducting quantum processor using a particular superconducting qubit, the transmon.

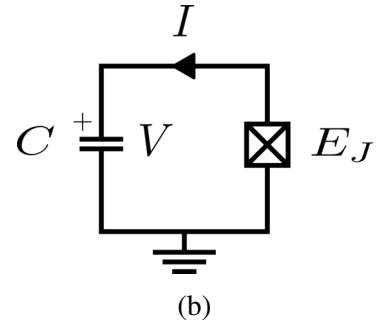
1.1 THE TRANSMON QUBIT

Superconducting qubits are essentially electrical oscillators. Conventional room-temperature electrical oscillators are made with linear components like inductors and capacitors. Let us consider an LC oscillator made with superconducting components (Capacitance C and Inductance L , see Fig. 1.1a). The energy of the system can be described as follows:

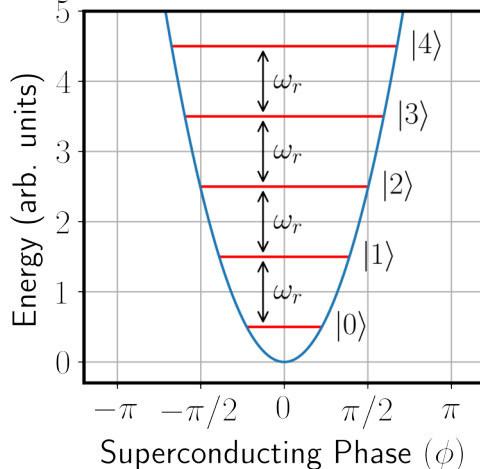
$$\mathcal{H} = \frac{Q^2}{2C} + \frac{\phi^2}{2L} \quad (1.2)$$



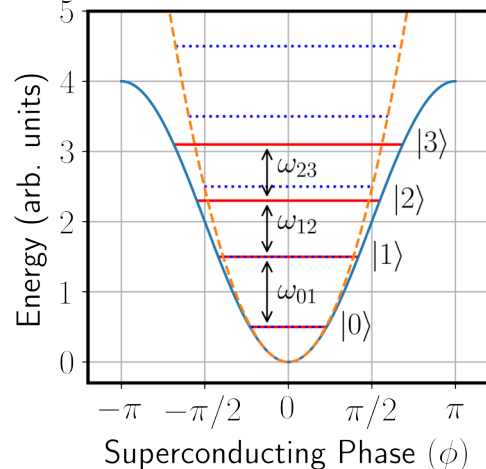
(a)



(b)



(c)



(d)

Figure 1.1: An illustration of the energy levels in superconducting oscillators **(a)** An LC oscillator **(c)** A transmon qubit, with Josephson energy E_J **(c)** Uniformly spaced energy levels of the LC oscillator. **(d)** Energy levels of the transmon qubit. The non-linear Josephson Junction creates the required anharmonicity to make sure that the lowest two energy levels can be used as a qubit. This is in contrast with the harmonic oscillator in **(c)**

Here, Q is the charge in the capacitor and ϕ is the flux in the inductor. We can see that Q and ϕ can be cast as canonical momentum and position variables, respectively:

$$\frac{\partial \mathcal{H}}{\partial Q} = \frac{Q}{C} = V = -L \frac{\partial I}{\partial t} = -\dot{\phi} \quad (1.3)$$

$$\frac{\partial \mathcal{H}}{\partial \phi} = \frac{\phi}{L} = I = \dot{Q} \quad (1.4)$$

We can choose the direction of the current so as to create the necessary Poisson bracket (later, commutation relation structure). We observe that we can quantize $Q \rightarrow \hat{Q}$ and $\phi \rightarrow \hat{\phi}$ and set $[\hat{Q}, \hat{\phi}] = -i\hbar$. We now clearly see that the Quantum Hamiltonian is of

the form of a harmonic oscillator, yielding uniformly spaced energy levels as shown in Fig. 1.1c. We can define the Hamiltonian in terms of ladder operators as:

$$\hat{H} = \hbar\omega_r \left(\hat{a}^\dagger \hat{a} + \frac{1}{2} \right) \quad (1.5)$$

Where

$$\omega_r = \frac{1}{\sqrt{LC}}, \quad Z_c = \sqrt{\frac{L}{C}}, \quad \hat{a} = \frac{1}{\sqrt{2\hbar Z_c}}(\hat{\phi} + iZ_c\hat{Q}) \quad (1.6)$$

Here, ω_r is the frequency of the oscillator (resonator), and Z_c is the characteristic impedance.

However, as we can see in Fig. 1.1c, the levels are spaced uniformly. Due to this, we can't address any specific two-level subspace. If we drive the oscillator at the oscillator's frequency, we will end up creating a coherent state, and we will be unable to create qubit states without some form of non-linearity. We do this by introducing the crucial element for superconducting quantum processors, the Josephson junction.

1.1.1 Hamiltonian of a Single Transmon Qubit

A Josephson junction is a circuit element made by sandwiching an insulating junction between two superconducting nodes. As shown in Fig. 1.1b, a transmon qubit is constructed by shunting a Josephson junction with a large capacitance. This ensures that the qubit is insensitive to charge noise (Koch *et al.* (2007)). Charge noise is the sensitivity of the eigen energies of the qubit to stray charge present in the capacitance of the circuit.

The Josephson junction functions as a non-linear inductor. Its energy-current relation takes the form:

$$E = E_J(1 - \sqrt{1 - (I/I_c)^2}) = E_J(1 - \cos \delta) \quad (1.7)$$

where I_c is the critical current of the Josephson Junction, $E_J = I_c\Phi_0/2\pi$ is the Josephson Energy (Φ_0 is the superconducting flux quantum), and $\delta = \phi/\Phi_0$ is the normalized superconducting phase across the junction.

This transforms the Hamiltonian of the oscillator into the form:

$$\hat{H} = \frac{\hat{Q}^2}{2C} + E_J(1 - \cos \hat{\delta}) \quad (1.8)$$

For convenience, we define $\hat{n} = \hat{Q}/2e$ as the number operator (number of Cooper pairs crossing the junction) and $E_C = e^2/2C$, where C is the total capacitance across the junction. Thus, the Hamiltonian now becomes:

$$\hat{H} = 4E_c\hat{n}^2 - E_J \cos \hat{\delta} \quad (1.9)$$

The transmon regime is defined to be the point where $E_J/E_C \geq 50$. This allows the qubit to be robust to charge variation (\hat{n} becomes offset as $\hat{n} - n_g$, due to n_g stray Cooper pairs). This allows much larger coherence times than the charge qubit, from which the transmon qubit is derived.

The spectrum of the transmon qubit is shown in Fig. 1.1d, which shows how the energy levels have slightly more anharmonicity than those of a harmonic oscillator. The anharmonicity of the transmon is defined as:

$$\alpha = \omega_{12} - \omega_{01} \quad (1.10)$$

This quantity is negative for transmon qubits, since $\omega_{12} < \omega_{01}$.

Since we are operating in a regime where $E_J \gg E_C$, we can expand the cosine term in the Hamiltonian (Eq. 1.9) for low energy states:

$$\hat{H} = 4E_c\hat{n} - E_J\left(1 - \frac{\hat{\delta}^2}{2} + \frac{\hat{\delta}^4}{24} - O(\hat{\delta}^6)\right) \quad (1.11)$$

Eliminating fast rotating terms (Non-excitation preserving terms, this is also called a rotating wave approximation or RWA), we can show that the transmon Hamiltonian is well approximated by a Duffing oscillator Hamiltonian of the form (upto constants):

$$\hat{H}/\hbar = \omega_T a^\dagger a + \frac{\alpha}{2} a^\dagger a a^\dagger a \quad (1.12)$$

Here, $\omega_T = (\sqrt{8E_J E_C} - E_C)/\hbar$ is the qubit's transition frequency and $\alpha = -E_C/\hbar$ is the anharmonicity. The exact solution of a transmon needs to be estimated using Mathieu functions, but for the purposes of our study, the Duffing oscillator approximation is used.

1.2 QUANTUM GATES ON TRANSMON QUBITS

Now that we have set up the framework for the analysis of a transmon qubit, we will now analyze how single-qubit gates and two-qubit gates are implemented for such qubits. This can either be a microwave drive coupled to the qubit or a change of the flux in the system, which changes the parameters of the qubit. In general, creating gates with microwave drives allows for a simpler design since extra flux lines are not needed.

Microwave drives are generally implemented by coupling an electromagnetic drive to the qubit. In general, the drive is coupled capacitively to the qubit, as shown in Fig. 1.2a. The dynamics of this evolution are discussed in the subsection below.

1.2.1 Single Qubit Gates: Rabi Oscillations

As shown in Fig. 1.2a, the drive is coupled capacitively to the qubit. We can write down the Hamiltonian as (Krantz *et al.* (2019)):

$$\hat{H} = \hat{H}_Q + \frac{C_c}{C_c + C_Q} V_d(t) \hat{Q} \quad (1.13)$$

Here, the first term represents the transmon qubit's raw Hamiltonian (Eq. 1.12) and the second term represents the coupling term. From the definition of a, a^\dagger , we know that:

$$\hat{Q} = -i \sqrt{\frac{\hbar}{2Z_c}} (a - a^\dagger) \quad (1.14)$$

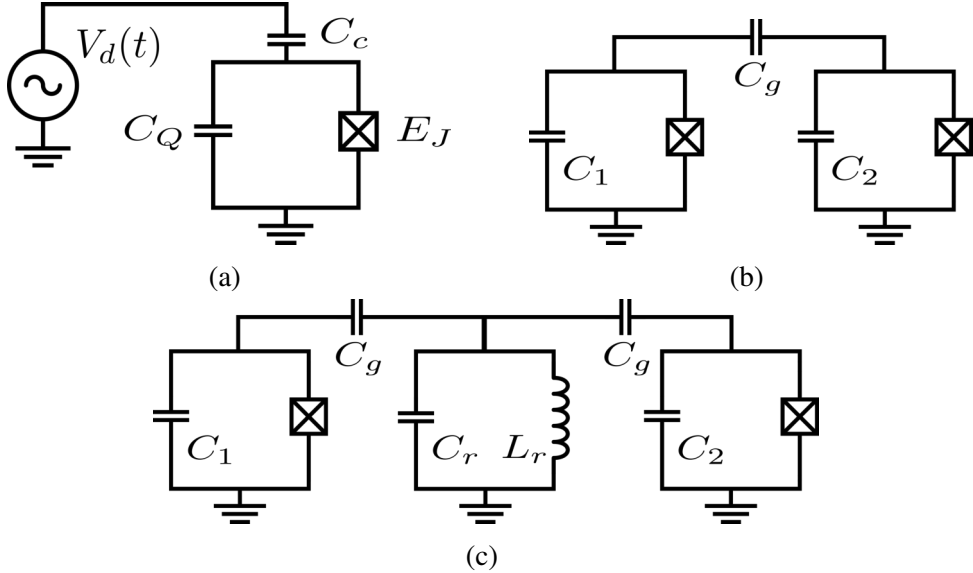


Figure 1.2: Circuit representations of (a) Driving a transmon qubit (b) Capacitively coupling two transmon qubits (c) Mediating the coupling between two transmon qubits with a resonator

Thus, if we truncate the subspace to the two levels of the qubit, the Hamiltonian simplifies to:

$$\hat{H}/\hbar = -\frac{\omega_T}{2}\hat{\sigma}_Z + kV_d(t)\hat{\sigma}_Y \quad (1.15)$$

Here, k incorporates all relevant scaling factors. To analyze this evolution better, we can move into the rotating frame (RF) of the qubit, by transforming all vectors with $U = e^{i\hat{H}_Q t}$, which cancels the evolution due to the static qubit Hamiltonian. This gives us:

$$\hat{H}_{\text{RF}}/\hbar = kV_d(t) (\cos(\omega_T t)\hat{\sigma}_Y - \sin(\omega_T t)\hat{\sigma}_X) \quad (1.16)$$

We now set $V_d(t) = I(t) \cos(\omega_d t) + Q(t) \sin(\omega_d t)$, where the drive has quadratures $I(t), Q(t)$ and is modulated on a carrier of frequency ω_d . We set $\omega_d = \omega_T$ (driving on resonance). Simplifying the Hamiltonian, and neglecting terms which rotate with high frequency ($\omega_d + \omega_T$), we get:

$$\hat{H}/\hbar = \frac{k}{2}(I(t)\hat{\sigma}_Y - Q(t)\hat{\sigma}_X) \quad (1.17)$$

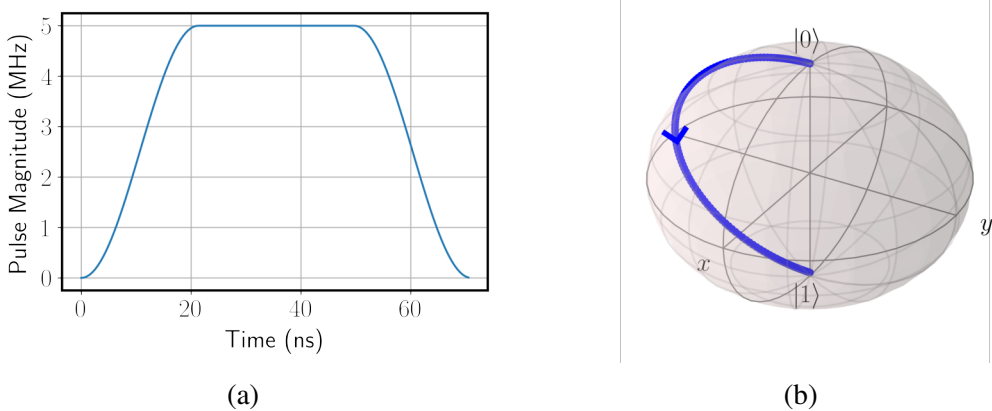


Figure 1.3: Evolution of a single transmon qubit under a Q-quadrature drive. The pulse shape is shown in (a). (b) evolution of the qubit state, as plotted on the Bloch Sphere. We can see how the qubit state starts at the pole and rotates about the X-axis. This is an example of a π pulse, where the qubit undergoes a bit flip

Thus, we can see that the I quadrature produces rotations about the Y-axis, and the Q quadrature produces rotations about the X-axis. This evolution is shown in Fig. 1.3. When the evolution is carried out till the qubit reaches the other pole (implementing a bit flip gate), it is called a π pulse. Rotations about the Z-axis can be carried out at the software level by changing the phase reference for that qubit (Krantz *et al.* (2019)), since the qubit Hamiltonian itself has an $\omega_T \hat{\sigma}_Z$ term. Thus, we can achieve any single-qubit gate by calibrating our pulse length and quadrature.

Without loss of generality, the I and Q quadratures are interchangeable. Thus, throughout the rest of this thesis, we will model the drive as follows:

$$\hat{H}_{\text{drive}}/\hbar = (I(t) \cos(\omega_d t) + Q(t) \sin(\omega_d t))(a + a^\dagger) \quad (1.18)$$

1.2.2 Coupled Transmon Qubits and Two Qubit Gates

For a complete quantum gate set, we also need two-qubit gates, like the CNOT gate. For implementing such gates, we need to enable photon exchange between transmon qubits. This can be done in a variety of ways. The most common way is to use either a bus

resonator (Fig. 1.2c) or couple the qubits capacitively (Fig. 1.2b).

To derive the Hamiltonian of the coupling term, we shall consider the case where the two transmons are capacitively coupled (Fig. 1.2b). The energy of the coupling capacitance is given by $0.5 * C_g * (V_1 - V_2)^2$. However, the terms with $C_g V_1^2, C_g V_2^2$ can be incorporated as effective capacitances in the individual qubits. Thus, the interaction term is of the form $H_{\text{int}} = gV_1V_2$. Since $V \propto Q$, we can write $H_{\text{int}} = g(a_1 - a_1^\dagger)(a_2 - a_2^\dagger)$. Subsequently, we apply the rotating wave approximation to eliminate fast rotating terms $(a_1^\dagger a_2^\dagger, a_1 a_2)$. This yields a Hamiltonian of the form:

$$\hat{H}/\hbar = \hat{H}_{T1} + \hat{H}_{T2} + g(a_1^\dagger a_2 + a_2^\dagger a_1) \quad (1.19)$$

It can also be shown (Magesan and Gambetta (2020)) that coupling mediated by a resonator is equivalent to a direct capacitive coupling, provided that the qubit frequencies are detuned from the resonator frequency.

Now that we know the form of the Hamiltonian of coupled transmon qubits, we will briefly see how entangling gates are implemented. The most popular two-qubit gate for fixed-frequency transmon qubits is the Cross Resonance (CR) Gate (Chow *et al.* (2011)). This will be the gate that the remainder of this thesis will focus on. This gate involves driving the control qubit at the frequency of the target qubit. Due to the non-linearity of the transmon, this causes rotations in the target, whose direction depends on the state of the control. This is discussed in detail in Chapter 2.

1.3 THESIS OUTLINE

The main goal of this thesis is to demonstrate a toolkit for the analysis of quantum processors with a given connectivity. These tools were built for a fixed-frequency transmon qubit architecture. The most convenient two-qubit gate in such architectures is the Cross Resonance Gate. The dynamics of this gate, fidelity, sources of error are

discussed in detail in Chapter 2.

One of the goals of this project is to optimize and characterize a 7-qubit processor being built in our group. The CR gate imposes certain constraints on the frequencies of the qubits in a connected network. Besides this, nanofabrication of qubits leads to inevitable spreads in qubit frequencies. To find sweet spots for qubit frequencies, which are robust to such variations, the tools developed in Chapter 2 are applied to this 7-qubit processor. This is discussed in detail in Chapter 3.

Fabrication of qubits requires the design of qubit chips. Our 7-qubit processor is housed in two 3D ring resonators connected by a $\lambda/2$ resonator (Hazra *et al.* (2021)). For designing the qubits for optimum coherence time, inter-qubit coupling, gate time, readout time, and required anharmonicity, finite element simulations need to be performed. These classical electromagnetic simulations give us a lot of information about various design parameters. These design choices and simulations are discussed in Chapter 4

Finally, future directions for this research are discussed in the conclusion, Chapter 5.

CHAPTER 2

THE CROSS RESONANCE GATE

The Cross Resonance (CR) gate (Rigetti and Devoret (2010); Chow *et al.* (2011)) is a remarkable two-qubit gate due to its simple implementation. It is an all microwave gate in the sense that it just requires a microwave pulse to be applied and does not require any flux tuning in the circuit. In this chapter, we discuss the Hamiltonian of the gate, the dynamics, calibration, fidelity, and sources of error. We also develop a toolkit to study multi-qubit networks in which the native two-qubit gate is the CR Gate.

2.1 SYSTEM HAMILTONIAN

The CR gate is implemented by driving the control qubit (frequency ω_c) at the frequency of the target qubit ω_t . The control and target qubits are permanently coupled by a coupling element which is either a capacitor or a resonator detuned from the qubits' frequencies (See Fig. 2.1). This can be modelled as a direct qubit-qubit exchange coupling J (Magesan and Gambetta (2020)) (See Eq. 2.3). Such a drive causes rotations of the target qubit, whose rates depend on the state of the control qubit. This can be used to cause a separation between the states of the target when the control is in $|0\rangle$ vs $|1\rangle$ (see Fig. 2.2). This separation can be calibrated to π . However, to convert the CR gate to a CNOT gate, we need single-qubit rotations, echo sequences, or active cancellation (Sheldon *et al.* (2016)).

The system's Hamiltonian (unless specifically mentioned, all Hamiltonians in this thesis will be represented in units of frequency, by dividing by \hbar throughout) can be described as follows:

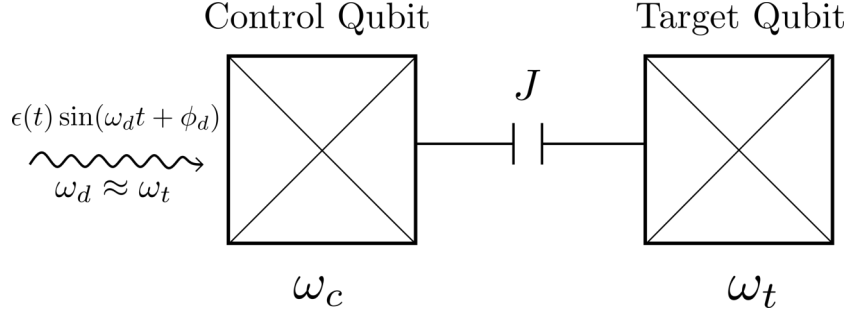


Figure 2.1: A schematic representation of the CR gate. The control and target qubit are coupled by a resonator element (which can be reduced to an effective capacitive coupling). There is a microwave drive of frequency $\omega_d \approx \omega_t$ applied on the control, which causes state dependant Rabi oscillations in the target

$$\hat{H} = \hat{H}_q + \hat{H}_c + \hat{H}_d \quad (2.1)$$

Here, \hat{H}_q , \hat{H}_c , \hat{H}_d represent the Hamiltonian of the transmon qubits, the coupling terms and the drive respectively. The qubit Hamiltonian \hat{H}_q is given by the Duffing oscillator expansion of the transmon (Eq. 1.12), which approximates it as a mildly non-linear oscillator with $|0\rangle \rightarrow |1\rangle$ transition frequency ω and anharmonicity α . Anharmonicity is defined as $\alpha = \omega_{1\rightarrow 2} - \omega_{0\rightarrow 1}$.

$$\hat{H}_q = \sum_{i=c,t} \omega_i \hat{a}_i^\dagger \hat{a}_i + \alpha_i \hat{a}_i^\dagger \hat{a}_i (\hat{a}_i^\dagger \hat{a}_i - \hat{I}) \quad (2.2)$$

Here, \hat{a}_i , \hat{a}_i^\dagger are annihilation and creation operators respectively. The permanent coupling is given by an exchange Hamiltonian of the form

$$\hat{H}_c = J(\hat{a}_c^\dagger \hat{a}_t + \hat{a}_t^\dagger \hat{a}_c) \quad (2.3)$$

where J is the exchange coupling strength. The control qubit's time dependent drive Hamiltonian is given by (Transformed from Eq. 1.18)

$$\hat{H}_d = \epsilon(t) \hat{a}_c + \epsilon^*(t) \hat{a}_c^\dagger \quad (2.4)$$

where $\epsilon(t) = \Omega(t)e^{i\omega_d t}$ is the time-dependent pulse shape, with $\Omega(t)$ representing the pulse's amplitude and ω_d representing the drive frequency.

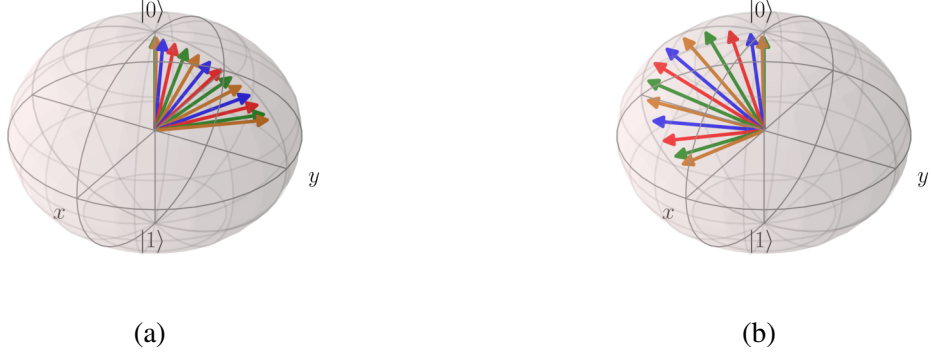


Figure 2.2: A visualization of the CR gate. The target qubit rotates about the X-axis to a different extent when the control is in $|0\rangle$ as shown in **(a)** vs when the control is in $|1\rangle$, as shown in **(b)**

2.2 EFFECTIVE HAMILTONIAN THEORY

Initial theoretical studies of the CR Gate approximated the transmon as a two-level system, studying only the computational subspace. However, there is significant involvement of higher levels in this gate implementation. Using techniques such as Schrieffer-Wolff perturbation theory or the principle of least action (Magesan and Gambetta (2020); Malekakhlagh *et al.* (2020)), the effective Hamiltonian of this gate in the computational subspace can be shown to be of the form:

$$\hat{H}_{\text{eff}} = \omega_{IX} \frac{\hat{I}\hat{X}}{2} + \omega_{ZX} \frac{\hat{Z}\hat{X}}{2} + \omega_{ZI} \frac{\hat{Z}\hat{I}}{2} + \omega_{IZ} \frac{\hat{I}\hat{Z}}{2} + \omega_{ZZ} \frac{\hat{Z}\hat{Z}}{2} \quad (2.5)$$

ω_{IX} causes state independent rotation of the target, while ω_{ZX} causes rotations in opposite directions depending on the state of the control qubit. These rotations are about the X-axis of the target. The difference in these two terms gives rise to the entangling gate, and these are desirable terms in our Hamiltonian. ω_{ZI} is the Stark Shift of the control qubit, caused by off-resonant drive. This causes a phase accumulation and can be corrected by applying echo sequences. ω_{ZZ}, ω_{IZ} are coherent error terms, which cause

shifts in the plane of rotation. We need to have a high ratio of ω_{ZX}/ω_{ZZ} so that coherent error does not accumulate.

To understand the constraints imposed by these parameters, we can vary the control-target detuning $\Delta_{ct} = \omega_c - \omega_t$ and study the variations of these parameters with drive strength Ω . This variation is plotted in Fig. 2.3.

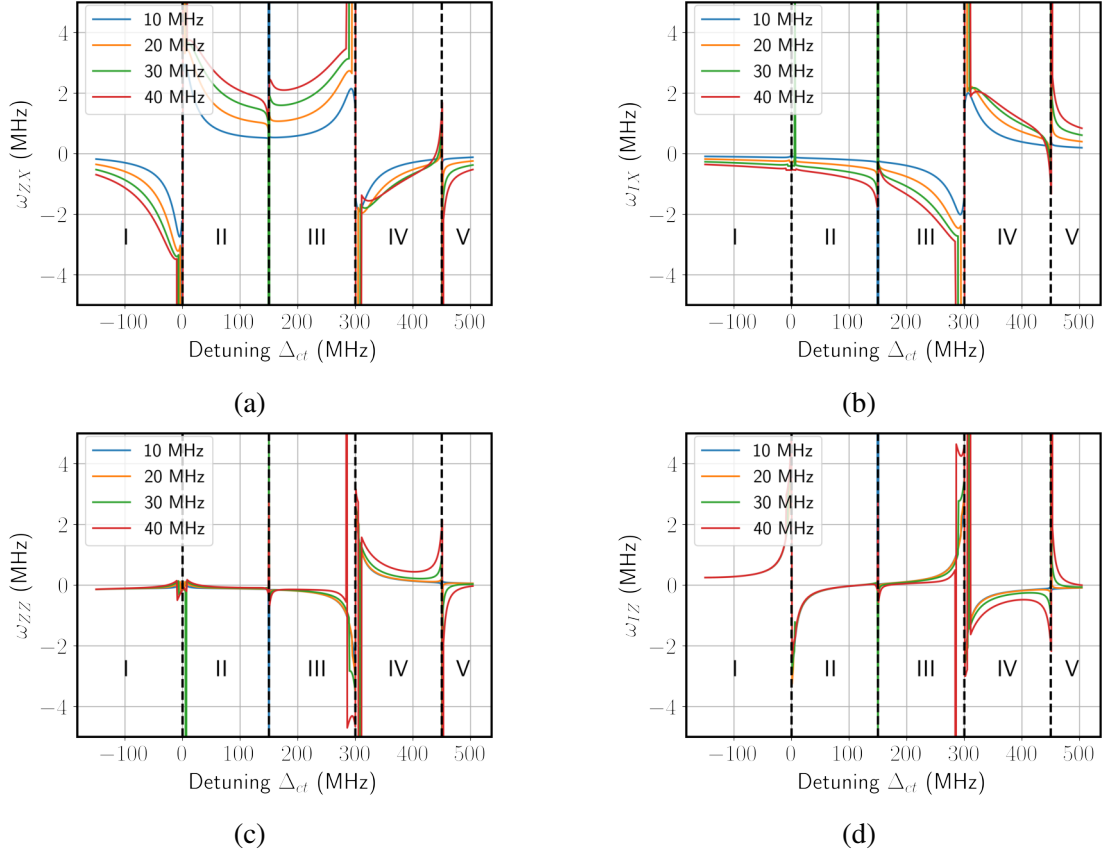


Figure 2.3: Effective Hamiltonian terms vs control-target detuning Δ_{ct} , for various drive strengths Ω . **(a)** ZX Rate **(b)** IX Rate **(c)** ZZ Rate **(d)** IZ Rate. There are poles at $\Delta_{ct} = \alpha_t, 0, -\alpha_c/2, -\alpha_c, -3\alpha_c/2$, which naturally divide the frequency landscape into five parts, as shown. The various curves represent different drives strengths Ω , as specified in the key. These are generated with coupling $J = 3$ MHz and anharmonicity $\alpha = -300$ MHz

We can see that there are multiple poles in the frequency landscape (Malekakhlagh *et al.* (2020)). These poles are caused by resonances between various transitions in the two qubits, as described in Table 2.1. These poles naturally divide the landscape into five

parts (see Fig. 2.3). Regions I, IV, V are not very good regions for operation since the rotation rates are slow. Ideally, we need to choose qubits in regions II, III for fast and accurate gates. Δ_{ct} needs to be chosen far away from the poles for optimum operation.

Resonant Transition	Matching Condition
$ 11\rangle n\rangle \leftrightarrow 02\rangle n\rangle$	$\Delta_{ct} = \alpha_t = -300 \text{ MHz}$
$ 01\rangle n\rangle \leftrightarrow 10\rangle n\rangle$	$\Delta_{ct} = 0 \text{ MHz}$
$ 00\rangle n\rangle \leftrightarrow 20\rangle n-2\rangle$	$\Delta_{ct} = -\alpha_c/2 = 150 \text{ MHz}$
$ 11\rangle n\rangle \leftrightarrow 20\rangle n\rangle$	$\Delta_{ct} = -\alpha_c = 300 \text{ MHz}$
$ 10\rangle n\rangle \leftrightarrow 30\rangle n-2\rangle$	$\Delta_{ct} = -3\alpha_c/2 = 450 \text{ MHz}$

Table 2.1: List of resonances which cause poles in the effective Hamiltonian. $|ij\rangle|n\rangle$ represents Control, Target and Drive Field in Fock states $|i\rangle, |j\rangle, |n\rangle$ respectively. $\alpha_c = \alpha_t = -300 \text{ MHz}$ has been taken as the typical value of anharmonicity for all the qubits.

Spectator qubits: Some more Constraints

When more qubits are added to the processor, there are more multibody resonances that come into play, which have to be taken into account. These can be detrimental to gate fidelity. For an example of the most important constraints that need to be taken into consideration, consider the schematic shown in Fig. 2.4

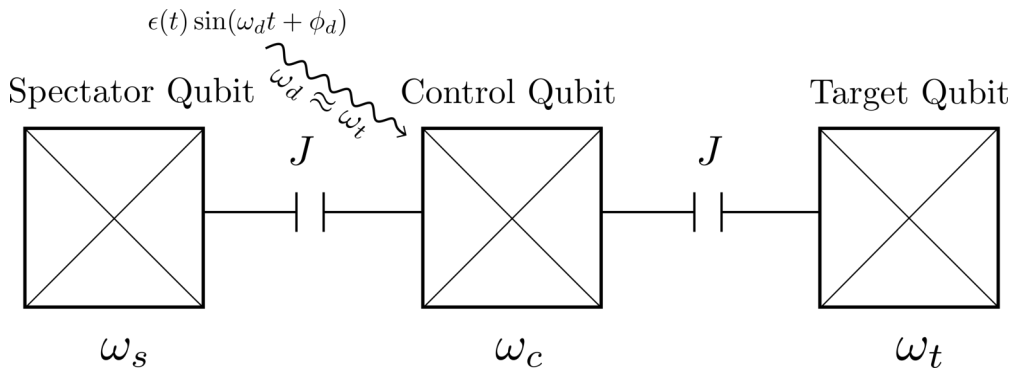


Figure 2.4: An example of a 3 qubit system, where the spectator and target qubits are coupled to the control qubit, with coupling strength J . They each have frequencies $\omega_s, \omega_t, \omega_c$ respectively. The Control-Target Cross Resonance Gate is driven by applying a pulse of frequency $\omega_d \approx \omega_t$. The resonances which arise from various frequency configurations are listed in Table 2.2

In such a configuration, there are other multiphoton processes that come into play that

affect gate fidelity (Malekakhlagh *et al.* (2020)). The matching conditions for these processes depend on the spectator target detuning Δ_{st} and the control target detuning Δ_{ct} . Some of these processes have been detailed in Table. 2.2.

Resonant Transition	Matching Condition
$ 101\rangle n\rangle \leftrightarrow 002\rangle n\rangle$	$\Delta_{st} = \alpha_t = -300$ MHz
$ 110\rangle n\rangle \leftrightarrow 020\rangle n\rangle$	$\Delta_{st} = \Delta_{ct} + \alpha_c = -230$ MHz
$ 100\rangle n\rangle \leftrightarrow 001\rangle n\rangle$	$\Delta_{st} = 0$ MHz
$ 100\rangle n\rangle \leftrightarrow 010\rangle n\rangle$	$\Delta_{st} = \Delta_{ct} = 70$ MHz

Table 2.2: List of 3 qubit resonances which cause poles in the effective Hamiltonian. $|ijk\rangle|n\rangle$ represents Spectator, Control, Target and Drive Field in Fock states $|i\rangle, |j\rangle, |k\rangle, |n\rangle$ respectively, according to Fig. 2.4. $\alpha_c = \alpha_t = \alpha_s = -300$ MHz has been taken as the typical value of anharmonicity for all the qubits. The Control-Target Detuning has been set to $\Delta_{ct} = 70$ MHz

2.3 CROSS RESONANCE GATE FIDELITY AND ERROR BUDGET

We can design parameters like Δ_{ct} based on first-order considerations like distance from the poles. However, a more powerful approach would be to estimate bounds on gate fidelity as a function of frequency configuration. The literature on this problem is extensive for 2 qubits (Magesan and Gambetta (2020); Malekakhlagh *et al.* (2020); Tripathi *et al.* (2019)). However, theoretical modeling of multi-qubit networks with CR gates has not been done so far, to the best of our knowledge. With this in mind, we developed a simulation framework to estimate the maximum possible gate fidelity.

Our approach is an extension of the method followed in Tripathi *et al.* (2019), since this method was most suited to an extension to multiple qubits. This approach involves Schrödinger time evolution based on the system Hamiltonian given in Eq. 2.1. The Unitary propagator obtained from time evolution can be compared to the ideal cross-resonance unitary and gives a measure of fidelity. We do not include decoherence in our simulations. Decoherence will demand that the drive strengths are higher and pulse lengths be smaller. However, increased drive strengths do not yield very significant improvements in pulse length since the effective Hamiltonian terms saturate (Eq. 2.5).

Thus, we can expect that the profile of the results extracted and frequency choices are a reasonable approximation of experiment (Tripathi *et al.* (2019)). We detail this method and the associated results below.

2.3.1 Time Evolution: Extracting and Analysing the Unitary Propagator

For a starting point for the analysis, we consider a two-qubit Hamiltonian, with only a Control and Target qubit. Extension to multiple qubits is discussed in Sec. 2.4. We first shift the system Hamiltonian (Eq. 2.1) to the frame rotating at the drive frequency ω_d . Note that this is a time-dependent Hamiltonian. The CR pulse is defined as follows:

$$\epsilon(t) = \begin{cases} E \frac{1-\cos(\pi t/\tau_r)}{2} & 0 \leq t \leq \tau_r \\ E & \tau_r \leq t \leq \tau_p - \tau_r \\ E \frac{1-\cos(\pi(\tau_p-t)/\tau_r)}{2} & \tau_p - \tau_r \leq t \leq \tau_p \end{cases} \quad (2.6)$$

The pulse shape is shown in Fig. 2.5. This consists of a flat middle part of amplitude E and a rise and fall time defined as a fraction of the pulse length ($\tau_r = f\tau_p$). This gives us the additional functionality of measuring gate fidelity as a function of the pulse shape too. For the purposes of our simulation, we choose $f = 0.3$, which allows for a smooth pulse and higher gate fidelity. Rapid pulses cause populations to shift to higher levels, or leakage, and this degrades gate fidelity.

We now choose 4 levels for both the transmon qubits, which yields a Hilbert space of dimension $4 \times 4 = 64$. Time evolution yields a unitary matrix U of dimensions 64×64 (See A.2). Since we are only computing fidelity in the computational subspace, we project this matrix into the computational subspace spanned by $|00\rangle, |01\rangle, |10\rangle, |11\rangle$, to get a matrix M of dimensions 4×4 .

We determine the fidelity of the gate by finding the distance of M from the closest ideal Cross-Resonance Unitary matrix. The ideal CR unitary matrices belong to the family of matrices of the form:

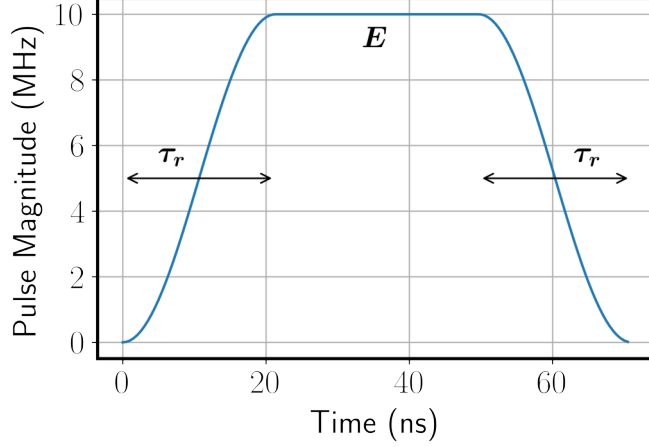


Figure 2.5: The pulse is represented in the frame rotating at drive frequency ω_d , which allows us to analyze only the magnitude. The pulse has length τ_p , maximum drive strength E , and a rise time $\tau_r = f\tau_p$, where f is the fraction of the pulse length occupied by the rising and falling regions, see Eq. 2.6

$$\mathcal{U}_{CR} = e^{i\theta_0} |0\rangle \langle 0|_c e^{-i\phi_0 \hat{X}_t/2} + e^{i\theta_1} |1\rangle \langle 1|_c e^{-i\phi_1 \hat{X}_t/2} \quad (2.7)$$

This is based on the requirement that the control qubit is unaffected except for a phase, and that the target qubit rotates only about the X-axis in the Bloch Sphere (see Fig. 2.2). The numbers θ_0, θ_1 denote the phases accumulated by the control when it is in state $|0\rangle, |1\rangle$ respectively. ϕ_0, ϕ_1 denote the different angles by which the target is rotated about the X-axis, when the control is in state $|0\rangle, |1\rangle$ respectively. It is this difference which gives rise to the entangling operation of this gate.

The matrix M might not even be completely unitary, if there is leakage outside the computational subspace. Also, error terms in the CR Hamiltonian (see Eq. 2.5) like ω_{ZZ}, ω_{IZ} might cause the target to rotate about a slightly different axis, resulting in gate infidelity. To capture all this, we extract parameters $\theta_0, \theta_1, \phi_0, \phi_1$ from M , to find the closest unitary U_{CR} belonging to the family described by Eq. 2.7. For 2 qubits, analytical expressions exist for these numbers (See A.1.1):

$$\phi_0 = -\text{angle} \left(\frac{M_{00} + M_{11} + M_{01} + M_{10}}{M_{00} + M_{11} - M_{01} - M_{10}} \right) \quad (2.8)$$

$$\phi_1 = -\text{angle} \left(\frac{M_{22} + M_{33} + M_{23} + M_{32}}{M_{22} + M_{33} - M_{23} - M_{32}} \right) \quad (2.9)$$

$$\theta_0 = \text{angle}[(M_{00} + M_{11}) \cos \phi_0/2 + i(M_{01} + M_{10}) \sin \phi_0/2] \quad (2.10)$$

$$\theta_1 = \text{angle}[(M_{22} + M_{33}) \cos \phi_1/2 + i(M_{23} + M_{32}) \sin \phi_1/2] \quad (2.11)$$

Now that we have identified the closest unitary U_{CR} with parameters $\theta_0, \theta_1, \phi_0, \phi_1$, we can now define fidelity as:

$$F_{MU} = \frac{\text{Tr}(M^\dagger M)}{d(d+1)} + \frac{|\text{Tr}(M^\dagger U)|^2}{d(d+1)} \quad (2.12)$$

Here, $d = 4$ is the dimension of the computational Hilbert Space. Intuitively, the first term in this expression can be thought of as capturing the "unitarity"; it measures leakage outside the computational subspace. The second term measures the overlap between the expected final states and the obtained final states, averaged over all initial states (Zanardi and Lidar (2004); Pedersen *et al.* (2007)). This is the fidelity in randomized benchmarking experiments.

2.3.2 Gate Time Calibration

Now that we have a definition of fidelity and a method to extract CR parameters from the propagator M , we can calibrate the gate. For obtaining a CR gate equivalent to a CNOT gate, we need to achieve $\phi_1 - \phi_0 = \pi$ (see Fig. 2.2), which means that the target states are antipodal on the Bloch Sphere, depending on the state of the control. After this, we can use single-qubit rotations to achieve a CNOT gate. To find the time taken to achieve a separation of π , we extracted ϕ_0, ϕ_1 for various pulse lengths τ_p for a given pulse amplitude E . A candidate plot is shown in Fig. 2.6a. The lines are extrapolated to find the point when the separation becomes π .

Thus, we are able to calibrate the gate for different drive strengths and obtain a plot of

CNOT gate time vs. drive strength, as shown in Fig. 2.6. We can see that the gate time reduces dramatically with E for the first 30 MHz but then saturates. This is because the Rabi rates in the effective Hamiltonian (See Eq. 2.5) saturate with drive strength. Once we have a table to calibrate the gate for different drive strengths, we can now measure the fidelity of the gate at different drive strengths to identify the optimal points of operation.

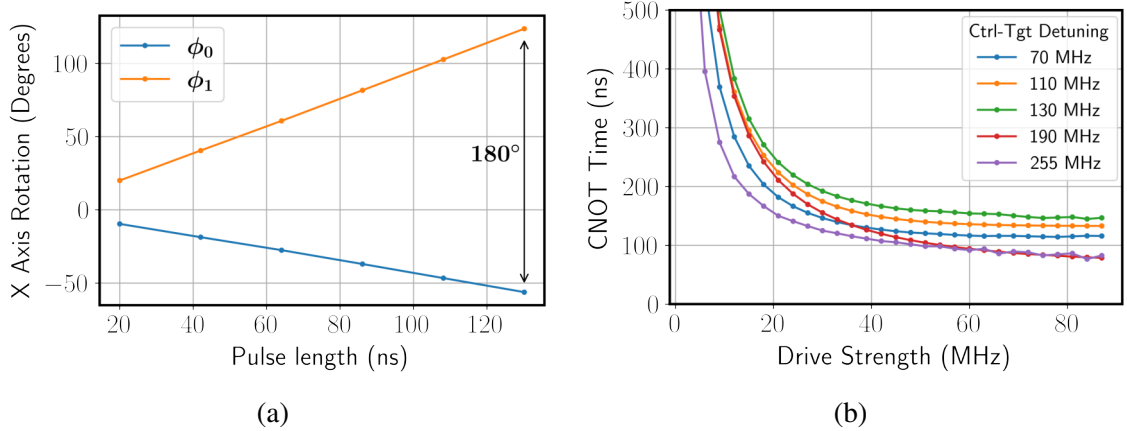


Figure 2.6: **(a)** ϕ_0, ϕ_1 for various pulse lengths τ_p for a given pulse amplitude E . The slope of the lines for ϕ_0, ϕ_1 yields the Rabi rates $\omega_{ZX} \pm \omega_{IX}$ (see Eq. 2.5). We extrapolate these lines and find the time τ_p when the separation becomes π . **(b)** Calibrating the CR gate, a plot of drive strength E vs required pulse time τ_p . Results are shown from various control-target detuning choices (Δ_{ct}), as shown in the legend. Coupling strength is fixed at $J = 3$ MHz

2.3.3 Fidelity and Sources of Error

After extracting the gate times at various drive strengths E , we can generate a plot of Gate Error, or $1 - F_{MU}$ (as per Eq. 2.12) vs. drive strength, when the CR gate is driven for the calibrated pulse length. This is shown for various detunings in Fig. 2.7. At low drive strengths, we get low gate fidelity due to the accumulated contribution of error terms like ω_{ZZ}, ω_{IZ} over the long gate times. At very high drive strengths, the sharp pulses cause leakage into higher levels of the transmons, and hence fidelity goes down. The ideal point of operation is located at the drive strength where gate time starts to saturate (See Fig. 2.6).

To get a measure of the sources of error in this gate, we next define various other families

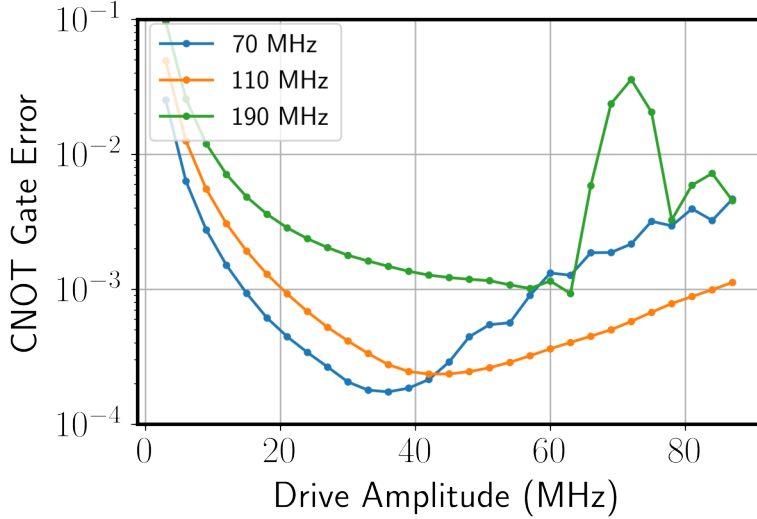


Figure 2.7: A plot of Gate Error ($1 - F$) vs Drive Strength (E) for various control-target detuning choices, as described in the legend. Coupling Strength is fixed at $J = 3$ MHz

of unitary matrices:

$$\mathcal{U}_T = |0\rangle\langle 0|_c U_0^t + |1\rangle\langle 1|_c U_1^t \quad (2.13)$$

In this family, the control is still unchanged, but the target is now allowed to undergo an arbitrary rotation in the computational subspace. Once again, we find the closest unitary U_T of the form Eq. 2.13 by using the matrix elements of M (obtained by projecting the unitary propagator). This is done by using the singular value decomposition (SVD). For any given matrix A , the SVD takes the form $A = U_A D V_A^\dagger$. It can be shown that the closest unitary matrix to A , which minimizes the norm $\|A - U\|$ is $U = U_A V_A^\dagger$. Thus, we take the elements of M along its block diagonal and perform SVD on each such block to compute U_0^t, U_1^t , which yields U_T . (Refer Appendix A)

We also find the closest unitary matrix to the propagator M by doing SVD directly on M . This gives us U_{CT} , a matrix where both the control and target are allowed to rotate arbitrarily. Note that each of these matrices relaxes the constraints (allowing arbitrary

rotations of the target and then control) on the unitary matrix one by one.

We first compute errors corresponding to each fidelities $E_{M,U} = 1 - F_{M,U}$, $E_{M,U_T} = 1 - F_{M,U_T}$, $E_{M,U_{CT}} = 1 - F_{M,U_{CT}}$ as per Eq. 2.12. Each of these terms contains information about one particular error:

- $E_{\text{CR}} = E_{M,U}$: The CR Gate Error
- $E_{\text{tgt}} = E_{M,U} - E_{M,U_T}$: This characterizes the error due to imperfect rotation (about Z or Y axis) of the target qubit. It measures the distance between the closest CR unitary (Target allowed to rotate only about the X axis) and the closest unitary M_T (target is allowed to rotate in any manner).
- $E_{\text{ctrl}} = E_{M,U_T} - E_{M,U_{CT}}$: This tells us the error due to rotation of the control. If the control rotates by any other form except a phase, this term will increase.
- $E_{\text{leak}} = E_{M,U_{CT}}$: This tells us the leakage error. Any distance between M and U_{CT} implies that the population left the computational subspace, since U_{CT} is the closest possible 2-qubit unitary matrix

We can see how these definitions allow us to create an "error budget":

$$E_{\text{CR}} = E_{\text{tgt}} + E_{\text{ctrl}} + E_{\text{leak}} \quad (2.14)$$

All these error terms are plotted in Fig. 2.8. We can see that our assumptions are justified; the error in low drive strengths is dominated by E_{rot} and the error in larger drive strengths is dominated by E_{leak} . At large drive strengths, the off-resonant drive on the control causes unwanted rotations, leading to the increase in E_{ctrl} .

2.4 EXTENSION TO MULTIPLE QUBITS

We now extend these tools to multiple qubits. In the effort to create a general simulation tool for CR gates, we create the following formalism for the Hamiltonian and for the evaluation of gate fidelity. Consider a system of N qubits, with a coupling matrix given by \mathbf{J} , where J_{ij} represents the strength of coupling between qubits i, j . Let us assume that we are driving a particular CR gate with qubit c being the control and qubit t being

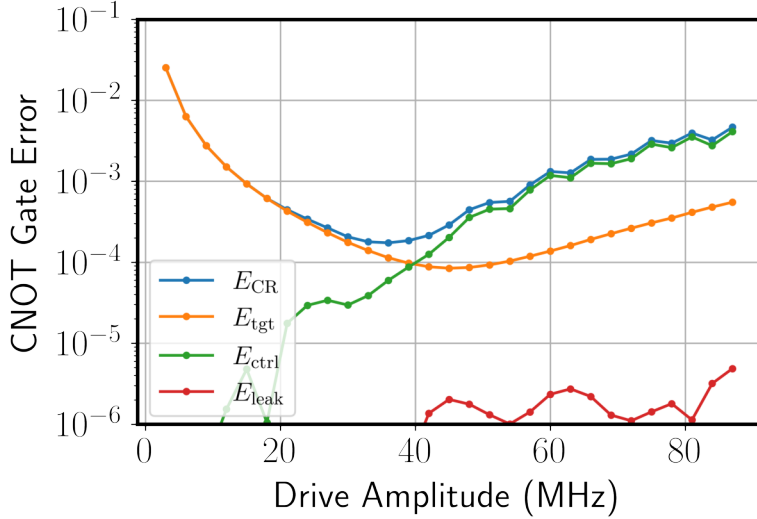


Figure 2.8: A plot of the error budget of the CR Gate, as a function of drive strength.

the target. The Hamiltonian for this is given by:

$$\hat{H}_{\text{sys}} = \hat{H}_q + \hat{H}_c + \hat{H}_d \quad (2.15)$$

$$\hat{H}_q = \sum_{i=1}^N (\omega_i - \omega_d) \hat{a}_i^\dagger \hat{a}_i + \alpha_i \hat{a}_i^\dagger \hat{a}_i (\hat{a}_i^\dagger \hat{a}_i - \hat{I}) \quad (2.16)$$

$$\hat{H}_c = \sum_{i=1}^N \sum_{j=1}^i J_{ij} (\hat{a}_i^\dagger \hat{a}_j + \hat{a}_j^\dagger \hat{a}_i) \quad (2.17)$$

$$\hat{H}_d = \epsilon(t) \hat{a}_c + \epsilon^*(t) \hat{a}_c^\dagger \quad (2.18)$$

Each annihilation and destruction operators have a tensor structure given by:

$$\hat{a}_i = \hat{I}_1 \otimes \hat{I}_2 \otimes \dots \hat{a}_i \otimes \dots \hat{I}_n \quad (2.19)$$

For computational tractability, we truncate all the operators to N_l levels. We then run the Schrödinger time evolution in the frame rotating at the drive frequency $\omega_d \approx \omega_t$. (This is why we use the term $\omega_i - \omega_d$ in the Hamiltonian).

Time evolution gives us a unitary propagator U , which is of dimensions $N_l^N \times N_l^N$. For notational simplicity, we can now permute the tensor order of this operator to make the

control and the target the last subspaces:

$$\mathcal{H}_{\text{sys}} = \mathcal{H}_1 \otimes \mathcal{H}_2 \otimes \dots \mathcal{H}_{\text{ctrl}} \otimes \mathcal{H}_{\text{tgt}} \quad (2.20)$$

\mathcal{H}_i represents the Hilbert space of qubit i . We then project this propagator into the computational subspace, to get a matrix M of dimensions $2^N \times 2^N$.

2.4.1 Constructing Relevant Families of Unitary Matrices

We next have to construct families of the form Eq. 2.7, 2.13 for multiple qubits, and evaluate the closest unitary matrices belonging to these families to identify gate fidelity and the error budget. Upto an overall phase, the ideal CR gate unitary family is given by:

$$\mathcal{U}_{\text{CR}} = \underbrace{(|0\rangle\langle 0|_1 + e^{i\theta_1}|1\rangle\langle 1|_1) \otimes (\dots \otimes (|0\rangle\langle 0|_c e^{-i\phi_0\hat{X}_t/2} + e^{i\theta_c}|1\rangle\langle 1|_c e^{-i\phi_1\hat{X}_t/2}))}_{\text{Spectator qubits}} \underbrace{\dots \otimes (|0\rangle\langle 0|_1 + e^{i\theta_1}|1\rangle\langle 1|_1) \otimes (\dots \otimes (|0\rangle\langle 0|_c e^{-i\phi_0\hat{X}_t/2} + e^{i\theta_c}|1\rangle\langle 1|_c e^{-i\phi_1\hat{X}_t/2}))}_{\text{Control, Target}} \quad (2.21)$$

Since we are operating in the rotating frame of the drive frequency, the target does not pick up a phase and rotates only about the X-axis. Note that this family's construction forces the target's rotation to depend only on the state of the control and not on the states of any other spectator qubit. The spectator qubits are also allowed to only pick up a phase since they are also expected to be unaffected by the CR gate. The list of numbers $(\theta_i) \quad i \in \{1, \dots, N - 2\}$ represents the relative phases picked up by the spectators.

In the above family (Eq. 2.21), the relative phase acquired by each qubit is independent of the states of the other qubits. To account for conditional phase (CP) errors, we define another family of matrices \mathcal{U}_{CP} , where the magnitudes of the matrix elements are the same as \mathcal{U}_{CR} . However, the phases are allowed to vary completely independently, allowing for conditional phase accumulation.

Next, we define the families of unitary matrices where n qubits are allowed to undergo

arbitrary rotations is given by:

$$\mathcal{U}^n = \begin{pmatrix} U_1^n & 0 & \dots \\ 0 & U_2^n & \dots \\ \vdots & \ddots & \vdots \\ 0 & 0 & U_{2^{N-n}}^n \end{pmatrix} \quad (2.22)$$

Here, each U_i^n is a $2^n \times 2^n$ (n qubit) unitary matrix. This structure works because the tensor order is as per Eq. 2.20. Thus, setting $n = 1$ allows only the target qubit to rotate arbitrarily. $n = 2$ allows both control and target to rotate. $n = 3$ onwards, each spectator qubit is allowed to rotate one by one. We do understand that these families allow rotation of the target, which is conditional on the states of the other spectators. However, this was chosen for numerical convenience and still detects errors accurately.

These families become larger and larger as n increases. This allows us to partition the error and detect which qubit is rotating badly. We sequentially allow more and more qubits to transform arbitrarily. Finally, when $n = N$, all N qubits are allowed to rotate arbitrarily, and we have an N qubit unitary. We shall call this matrix U_N .

Now, to find the error budget, we have to find the closest unitary to M (the propagator) from each of these families. This is not straightforward for multiple qubits. We have detailed our computational methods for this in the Appendix (see Sec. A.1.2).

With all these tools in place, we can now compute $E_{M,U_{CR}}$, E_{M,U^n} ($n \in \{1, 2, \dots, N\}$) using Eq. 2.12 (Note that $d = 2^N$ here). We then telescopically subtract the error due to larger and larger families, to get the error due to rotation of each qubit.

- $E_{CR} = E_{M,U_{CR}}$: The CR Gate Error
- $E_{CP} = E_{M,U_{CR}} - E_{M,U_{CP}}$: The conditional phase error. This detects conditional phase accumulation, caused by static ZZ error (See Sec. 3.1.2)
- $E_{tgt} = E_{M,U_{CP}} - E_{M,U^1}$: This characterizes the error due to imperfect rotation

(about Z or Y axis) of the target qubit.

- $E_{\text{ctrl}} = E_{M,U^1} - E_{M,U^2}$: This tells us the error due to rotation of the control. If the control rotates by any other form except a phase, this term will increase.
- $E_{\text{spec},i} = E_{M,U^{i-1+2}} - E_{M,U^{i+2}}$: This tells us the error due to rotation of spectator qubit i . We add 2 to both of the indices so as to account for the control and target qubit.
- $E_{\text{leak}} = E_{M,U_N}$: This tells us the leakage error. Any distance between M and U_N implies that the population left the computational subspace, since U_N is the closest possible N -qubit unitary matrix

Finally, the error budget is given by:

$$E_{\text{CR}} = E_{\text{CP}} + E_{\text{tgt}} + E_{\text{ctrl}} + \sum_{i=1}^{N-2} E_{\text{spec},i} + E_{\text{leak}} \quad (2.23)$$

2.5 MULTIPLE QUBITS - KEY RESULTS AND COMPARISON

To illustrate the use of the above tools on multi-qubit systems, we will consider a system of three qubits as shown in Fig. 2.4, where the spectator and target qubits are coupled to the control qubit. The control-target detuning is set to $\Delta_{ct} = 70$ MHz and the control-spectator detuning is set to $\Delta_{cs} = 110$ MHz.

To validate our numerical approach, we first check the calibration of the CR gate, following the approach in Sec. 2.3.2. The parameters ϕ_0, ϕ_1 , extracted from the unitary of the form Eq. 2.21 can be used to do this. A plot of the time taken to create a separation of π between the target states when the control is in $|0\rangle$ vs. $|1\rangle$ is shown in Fig. 2.9. It can be seen clearly that the time taken for the gate in the three-qubit system is almost identical to that in the two-qubit system for the given frequency choice.

Now that we have calibrated the CR gate, we compute a plot of drive strength E vs. Gate Error $E = 1 - F$ and compare it with the plot generated for two-qubits. This is shown in Fig. 2.10. We can see that the error in the three-qubit system is larger. This is explained by the fact that there are more constraints in the definition of fidelity for three qubits, in the sense that the spectator qubit also has to remain unaffected. Also, residual error terms

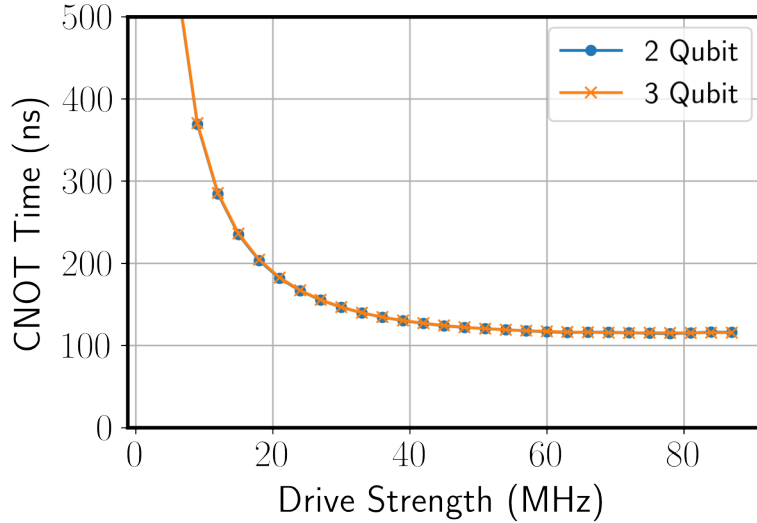


Figure 2.9: Calibrating the CR gate, a plot of drive strength E vs required pulse time τ_p . The results for a 2 qubit system and a 3 qubit system are shown. It can be seen clearly that there is a negligible difference between the two.

involving multiple qubits come into play. However, at values of drive strength where the gate error is minimum, we can see that the three-qubit and two-qubit errors are close.

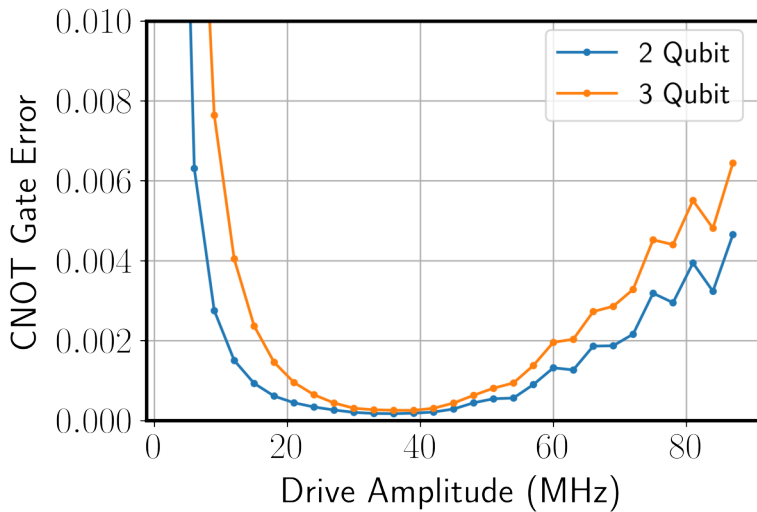


Figure 2.10: A plot of drive strength vs. Gate Error for three qubits and two qubits. We can see how the three-qubit gate error is higher than the two-qubit gate error. However, at drive strengths where the error is minimum, the two curves come close to each other.

Finally, we plot the error budget discussed in Sec. 2.4. This is shown in Fig. 2.11. The dip in the conditional phase error is explained by the fact that at minimum error, the propagator acquires the least conditional phase accumulation since the gate is fast enough, but the off-resonant drive on the control qubit is not too strong.

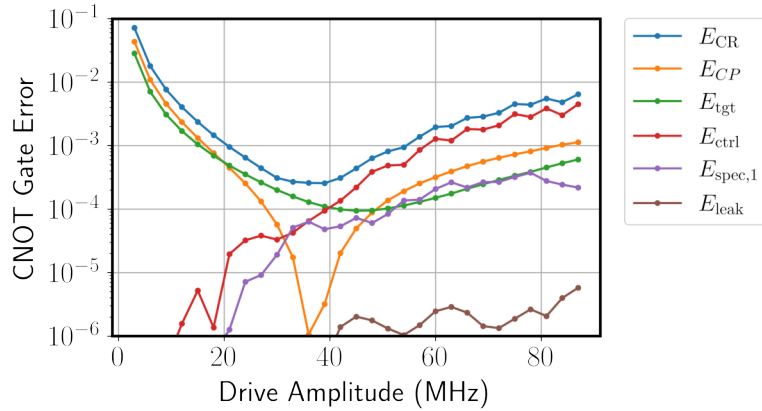


Figure 2.11: A plot of drive strength vs various error measures, for 3 qubits. At small drive strengths, the error is dominated by imperfect target rotation and phase accumulation. At large drives, leakage errors and unwanted qubit rotations dominate.

CHAPTER 3

OPTIMIZING MULTI-QUBIT NETWORKS

In this chapter, we shall apply the tools developed to analyze the CR gate to multi-qubit networks. In particular, we apply them to a seven-qubit processor with connectivity shown in Fig. 4.1c. We justify various design choices for the processor and test its robustness. We begin with a discussion of various coherent errors in connected qubit networks in Sec. 3.1. We then discuss the connectivity of the seven-qubit processor and candidate design choices in Sec. 3.2. Finally, we characterize the error budget and the variation of fidelity with spectator qubit detuning in Sec. 3.3.

3.1 CONSTRAINTS AND COHERENT ERRORS IN CONNECTED QUBIT NETWORKS

In any processor where the CR gate is the native entangling gate, there are certain constraints on the choices of qubit frequencies. Besides this, when transmon qubits are coupled capacitively or via a resonator, the coupling is always on. This causes state-dependent shifts in qubit frequencies, which we call Static ZZ error. We discuss these considerations in the subsections below.

3.1.1 Constraints Imposed by the Cross Resonance Gate

From the discussion in Sec. 2.2, 2.2, we have a list of the various poles in the frequency landscape. These are listed in tables 2.2 and 2.1. We know that choosing $0 < \Delta_{ct} < -\alpha$ is ideal, as they lie within regions II, III of the frequency landscape (See Fig. 2.3) (We shall choose all qubits to have an anharmonicity of α , since this is not a parameter that is tuned in general). Given such considerations, the most important constraints can be generalized as follows (Brink *et al.* (2018)):

- $\omega_i \neq \omega_j$ for any qubits i, j which are coupled
- $\omega_j - \alpha > \omega_i > \omega_j$ for any control i and target j . (For achieving a CNOT with target i and control j , we can just use single qubit Hadamard gates to transform the native CNOT gate)
- $\omega_i \neq \omega_j - \alpha/2$ for any control i and target j
- $\omega_i \neq \omega_j + \alpha$ for any two qubits i, j which are coupled
- $\omega_i \neq \omega_k$ for two target qubits i, k sharing a control qubit j
- $2\omega_j \neq \omega_k + \omega_i - \alpha$ control j , target k , and spectator qubit k coupled to control j

Given these constraints, when designing transmon processors, we have to choose frequencies for qubits that maximize distance from these poles. The more the connectivity of the processor, the harder it is to avoid these "frequency collisions." This is one of the reasons for IBM's movement toward processors with lesser connectivity, like the heavy hexagon lattice (Chamberland *et al.* (2020)), as compared to a rectangular grid lattice.

3.1.2 Static ZZ Error

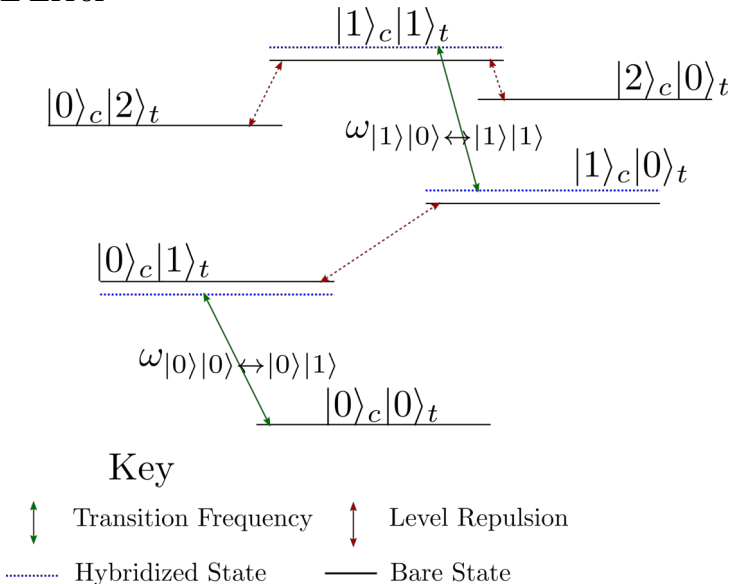


Figure 3.1: An energy level diagram to see how the static ZZ shift is caused by interaction between higher levels and the computational subspace. We consider a two qubit system with a control (c) and target (t) qubit coupled to each other. The key denotes various level repulsions and transition frequencies.

In any physical quantum processor, the computational Hilbert space is a subspace of the much larger Hilbert Space of the physical system. Thus, there will be interactions between the higher levels and the computational levels, causing coherent errors in the processor. The most significant error in permanently coupled qubit implementations is the static ZZ error. The ZZ shift is defined as:

$$\omega_{zz} = \omega_{|01\rangle \leftrightarrow |11\rangle} - \omega_{|00\rangle \leftrightarrow |10\rangle} \quad (3.1)$$

This difference (ideally zero), is caused by coupling between the states $|02\rangle, |11\rangle$ and between the states $|20\rangle, |11\rangle$ (In this explanation, we consider two coupled transmon qubits for simplicity). This coupling causes the frequency of each qubit to depend on the state of the other qubit, i.e. $\omega_{|00\rangle \leftrightarrow |10\rangle} \neq \omega_{|01\rangle \leftrightarrow |11\rangle}$ (See Fig. 3.1).

This difference is detrimental to processor performance since the qubit drives will have a frequency mismatch when neighboring qubits are in different states. During any computation, each qubit will be in an arbitrary state, resulting in arbitrary fluctuations of qubit frequencies. Besides this, the more the connectivity in the processor, the more ill-defined each qubit's frequency is. This is another reason why densely connected processors are harder to control accurately.

3.2 CHOOSING QUBIT FREQUENCIES IN THE 7 QUBIT PROCESSOR

Fig. 4.1c shows the connectivity in our 7 qubit processor. As we know from our discussion in Sec. 3.1, there are certain poles in the frequency landscape we need to avoid. The farther we are from the poles, the better the gate fidelity. We followed various approaches to settle upon a frequency configuration for the seven qubits. Initial approaches were based on manual trial and error. The main aim was to maximize the distance from all the poles in the list given in Sec. 3.1. This ensures high gate fidelity to the first order. After multiple iterations, we settled upon a few candidate frequency choices, as shown in Fig. 3.3.

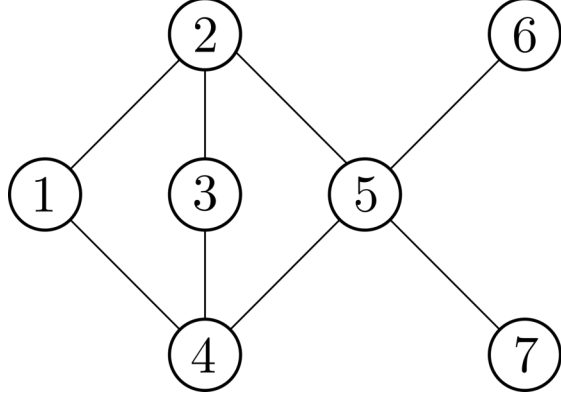


Figure 3.2: A depiction of the connectivity in the 7 qubit processor. Each edge in this graph represents an exchange coupling between the two qubits, of value around 3 MHz

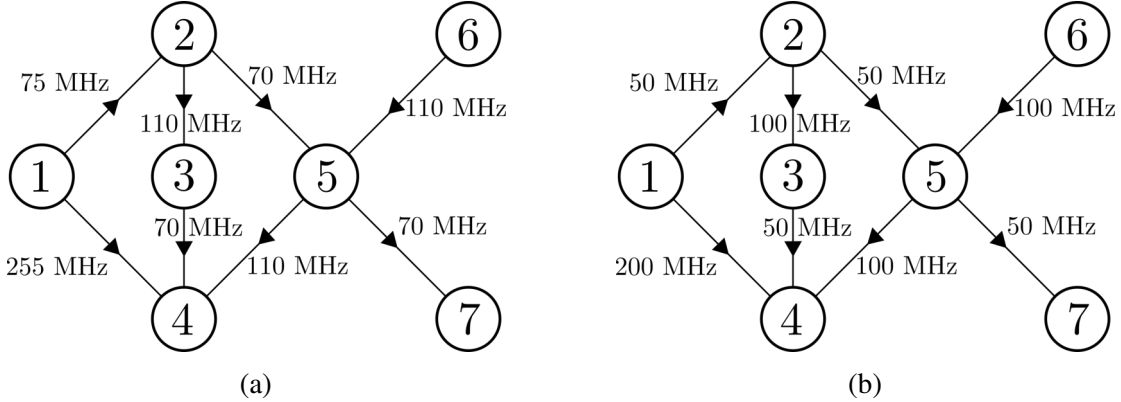


Figure 3.3: A candidate set of frequency choices for the seven qubits shown in Fig. 4.1c. The edges of the graph represent the detuning in frequency and the direction of the edge is towards the qubit with lower frequency **(a)** A candidate frequency choice with relatively higher detuning, allowing us to operate farther away from the poles. **(b)** A candidate frequency choice with lower detuning

3.2.1 Static ZZ Error in the 7 Qubit Processor

To have a measure of the ZZ-shifts in the processor, we computed the eigen states and eigen energies of the configurations given in Fig. 3.3a, 3.3b. This was done by computing the eigen values of the Hamiltonian of the processor, given by:

$$\hat{H}_{pr} = \hat{H}_q + \hat{H}_c \quad (3.2)$$

where \hat{H}_q, \hat{H}_c are given in equations 2.2, 2.3 respectively. Each qubit has 64 possible frequencies due to the 2^6 states of the other qubits. We find the mean transition frequency by averaging over all these values. We then plot the shifts of these 64 frequencies from the mean in Fig. 3.4 for each qubit. This gives us an idea of the spread in each qubit's frequency, which allows us to have a measure of the performance of the processor.

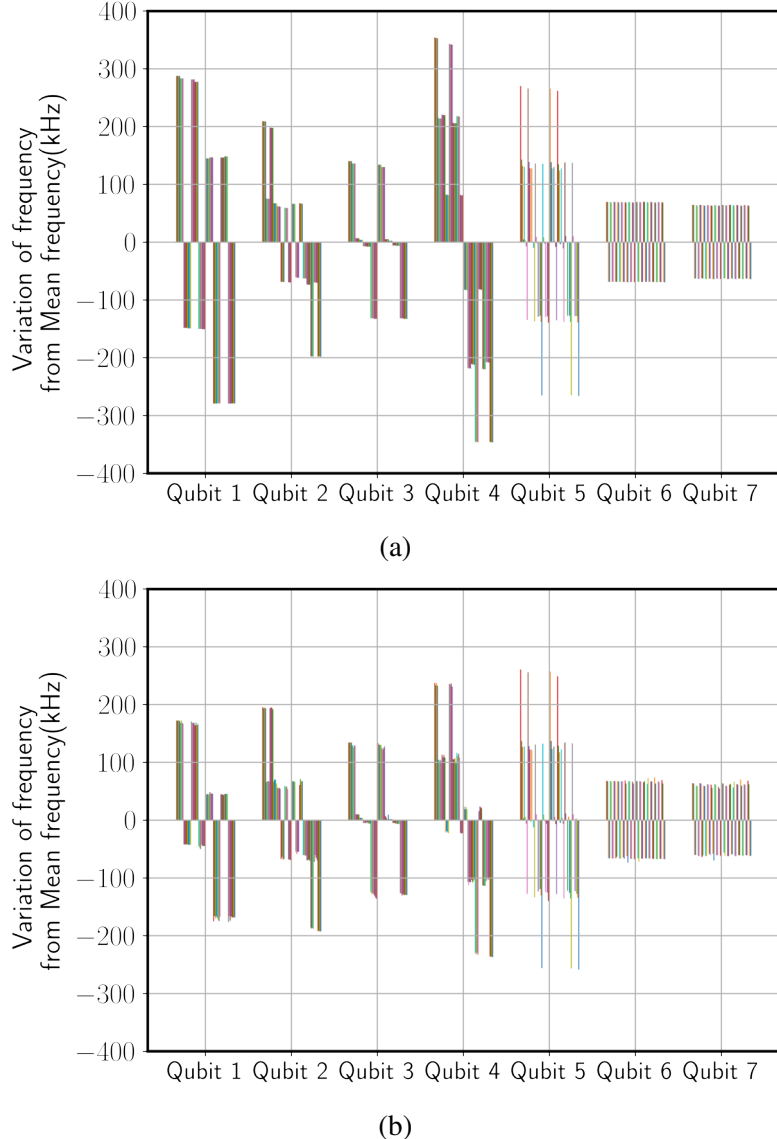


Figure 3.4: Static ZZ shifts for the 7 qubit processor. **(a), (b)** A measure of ZZ shifts for the frequency choices given in Fig. 3.3a and Fig. 3.3b respectively. The order of the ZZ shifts is around ~ 200 kHz. We can see that the ZZ shifts are larger for the frequency choice with a larger spread in qubit frequency. We can see that the most connected qubits (2,4,5) have the most variance in frequency, as opposed to qubits (1,3,6,7), owing to their sparse connectivity.

The gate interactions (ω_{ZX}, ω_{IX}) are an order of magnitude larger (See Sec. 2.2) than the static ZZ interactions. Thus, we can still drive CR gates without accumulating too much error. The final frequency configuration that we choose is given in Fig. 3.3a. Although the static ZZ shifts are higher for this particular configuration, the larger detuning allows for a larger ratio of ω_{ZX}/ω_{ZZ} , allowing higher fidelity gates. We observed this in our error budget calculation for various control-target detuning choices. (Note that the ω_{ZZ} referred to in this ratio is the dynamic ZZ term produced by the CR gate, see Sec. 2.2)

3.3 ERROR BUDGET ANALYSIS OF THE 7 QUBIT PROCESSOR

Having converged upon a set of candidate frequency choices, we now analyze the robustness of these choices to variations in qubit frequency. When transmon qubits are nanofabricated, there is an inevitable spread in the frequencies of the devices. This lowers the useful yield of the fabrication process. There is a need for a measure of how the fidelity will change as the frequencies of the qubits change. This will allow us to know if the qubits are usable by estimating a tolerance on the qubit frequency.

Another way of understanding whether our choices of frequencies are valid is by finding the error budget for all the 2 Qubit gates in the seven-qubit processor. However, simulating seven qubits at the same time is intractable with small-scale computing resources. A simpler way of estimating errors would be to consider a particular two-qubit gate in the processor and compute its error budget as each surrounding spectator qubit is added one by one. If there are no major changes in the gate fidelity, that justifies our frequency choice. Both the above analyses are described below.

3.3.1 Gate Fidelity vs Spectator Frequency

We can see from Fig. 3.3a that our frequency choices have only three detuning choices: 70 MHz, 110 MHz, and 255 MHz. (It is a fair assumption that the results for a detuning of 75 MHz won't vary much from results for 70 MHz). To estimate tolerance to Variation in frequency, we first consider a three-qubit system, as shown in Fig. 3.5a, where the

spectator is coupled to the control qubit. The control and target are detuned by 70 MHz, and a CR gate is driven between them. We then change the vary the detuning of the spectator from the control across a range of 540 MHz. At each point, we sweep the drive amplitude and identify the best possible fidelity achievable. We choose the drive frequency to be the mean of the various ZZ shifted frequencies of the target qubit so as to minimize static ZZ error. This is shown in Fig. 3.5a

We can see that there are various sweet spots where the gate error is minimum, as marked in pink. Any variation in frequency that places qubits somewhere in this region is still fine. We see that the choice of $\Delta_{CS} = 110$ MHz is particularly favorable, indicating that our choice of frequencies is good. Besides this, we can also see the various poles in the frequency landscape and how close we can get to them without degrading gate fidelity.

The poles that we see in Fig. 3.5a are as follows (See Tab. 2.2,2.1): **A** and **F** correspond two-photon processes, where $|\Delta_{CS}| + \Delta_{CT} = -\alpha$. This causes leakage from $|0\rangle \leftrightarrow |2\rangle$ for some qubits, which shows up in E_{leak} . **C** corresponds to the spectator and control being degenerate ($\Delta_{CT} = 0$). **D** corresponds to the spectator and target being degenerate ($\Delta_{CS} = \Delta_{CT} = 70$ MHz). These show up in the imperfect rotation of the target (E_{tgt}) and spectator ($E_{\text{spec},1}$) respectively. **B**, **E** correspond to other two photon processes, since $|\Delta_{CS}| = -\alpha/2$. The oscillations in the various components of errors are due to interferometric effects. This is because we sweep the drive strength and find the best drive strength for each frequency point. As we move away from each pole, the best drive strength oscillates to cancel the probability amplitude of the unwanted transitions.

We then repeat the same exercise, but the spectator is coupled to the target, as shown in Fig. 3.5b. We can see that the number of poles in the landscape is lower. This is because the spectator does not have a coupling with the driven qubit, the control. The poles in the landscape are as follows: **A**, **D** are two-photon processes, and **B**, **C** are degeneracies between the spectator and control and spectator and target, respectively.

We can extend this approach to other control-target detuning values of 110 MHz and 255 MHz. This will then cover every single control, target, and spectator combination in the seven-qubit processor, for our frequency choices. We then have an idea of the tolerance on qubit frequency for each gate. For the sake of brevity, the same plots for 110 MHz and 255 MHz are not shown here.

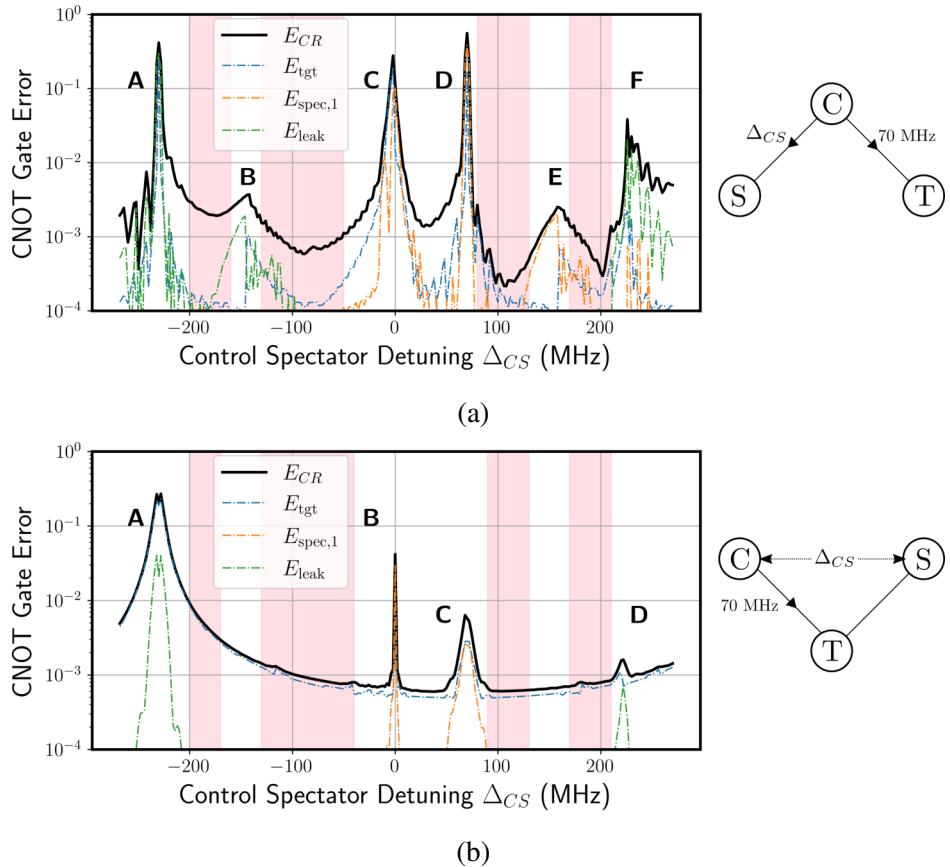


Figure 3.5: Variation in gate error with spectator detuning. The gate is driven between the control (C) and target (T) qubits, with the spectator coupled to the control qubit in (a) and coupled to the target qubit in (b). The various poles in the frequency landscape where gate error is high are labeled A-F. The contribution from various sources of error is shown in the legend. The pink regions indicate the spreads in frequencies that are tolerable. $\Delta_{CS} = \alpha(150\text{MHz}), -\alpha(-150\text{MHz})$ is always not considered, even if the gate fidelity there is high. This is because the spectator's two-qubit gate will have bad fidelity, despite high fidelity for the control-target gate. The most significant contributions to the error budget are also plotted, which show us the various processes causing the poles. The oscillations in these dashed lines are because the best drive strength at each of the points on the x-axis varies in an oscillatory manner.

3.3.2 Results on Cross Resonance Gates in Various Subsets

As we can see from the connectivity diagram (Fig. 4.1c), the most connected qubits are qubits 5 and 4 (or 2). If we can make sure that our frequency choices do not degrade the fidelities of the gates in which these qubits are involved, then we can be reasonably sure that the design choices made are correct.

We now consider CR gates on two different pairs of qubits. One is with qubit 5 as the control and qubit 7 as the target. We first analyze the fidelity vs. drive strength profile of just these two qubits. We then add qubits 4, 6, and 2 one by one and plot the fidelity vs. drive strength in the presence of these spectators. This is shown in Fig. 3.6. The order in which the qubits are added is shown in Fig. 3.6a. After this, the error comparison for systems with 2, 3, 4 and 5 qubits is shown in Fig. 3.6c. We can see that the error increases as the number of qubits increases. This is to be expected since the number of ZZ interactions increases with the number of qubits. However, we can see that the total error is still below 1%.

For drive amplitudes above 40 MHz, we can see that the error increases abruptly. This is attributed to a multiphoton process. To understand this better, we plot the most dominant contributions in the five-qubit error budget in Fig. 3.6e. This confirms that this is a multiphoton process involving qubit 6 and higher energy levels. However, we still have a good operating point below that drive strength for values of 20-35 MHz.

We next consider the CR gate with qubit 5 as the control and qubit 4 as the target. We then add qubits 2, 3, and 1 sequentially and repeat the same exercise as before. This is shown in Fig. 3.6b. The comparison between systems with 2, 3, 4, and 5 qubits in Fig. 3.6d shows us that the error does not increase dramatically and that there are good operating points with less than 2% error, even in the five-qubit system. Once again, there are some multiphoton processes at higher drive strengths, which can be seen in the five-qubit error budget analysis in Fig. 3.6f.

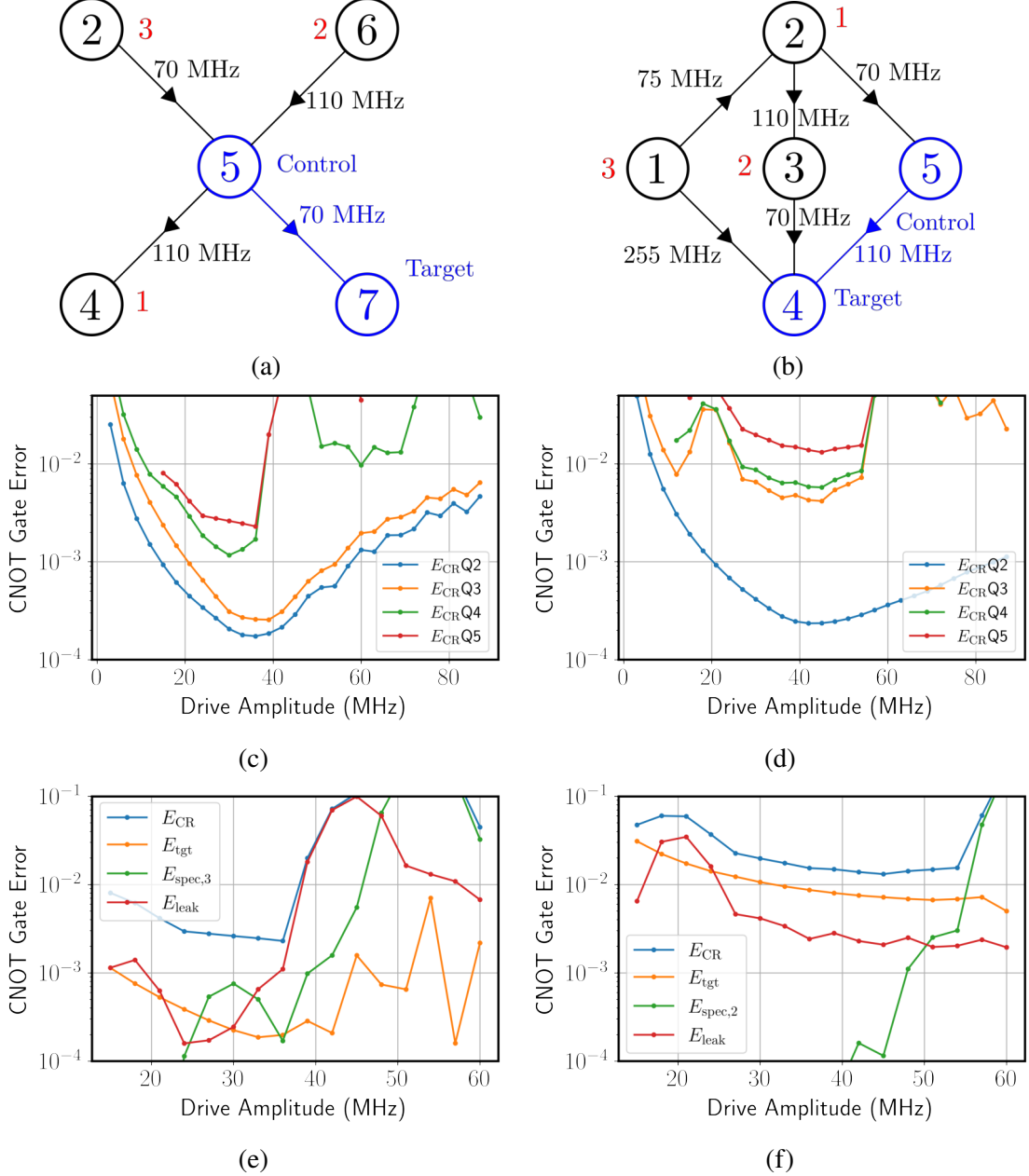


Figure 3.6: A study of the change in gate error as the size of the system increases. (a) and (b) indicate the two CR gates under consideration and also depict the order in which the spectator qubits are added. (c) and (d) depict the change in error in the systems in (a) and (b) respectively, as the system size increases. Q2 represents a system with 2 qubits, Q3 represents 3 qubits and so on. (e) and (f) represent the error budget for the 5 qubit systems and show the dominant contributions to the errors.

Finally, we analyse single qubit errors. The discussion in Sec. 2.4 is easily extended to the single qubit gates discussed in Sec. 1.2.1. Now, we drive the qubit under consideration on

resonance; this is at the mean of its own various ZZ shifted frequencies. The propagator is compared to the closest unitary of the form:

$$\mathcal{U}_{\text{RX}} = \underbrace{|0\rangle\langle 0|_1 + e^{i\theta_1}|1\rangle\langle 1|_1}_{\text{Spectator qubits}} \otimes (\underbrace{|0\rangle\langle 0|_2 + e^{i\theta_2}|1\rangle\langle 1|_2}_{\dots} \otimes \underbrace{e^{-i\phi\hat{X}_t/2}}_{\text{Target}}) \quad (3.3)$$

Here, 'RX' stands for rotation about the X-axis. The rest of the error budget is computed as discussed in Sec. 2.4.

This formalism is now extended to the most connected qubit, qubit 5. We drive an X rotation gate on qubit 5, to get a Hadamard gate (the angle of rotation is calibrated to $\pi/2$). We then calibrate this gate for various drive amplitudes. After this, the error budget is computed. We follow the same approach as in Fig. 3.6a, where we add qubits 7,4,6 and 2 one by one. The change in error as we add qubits is shown in Fig. 3.7a. We can see that we have error $< 0.1\%$ for even the five-qubit system. The error budget is shown in Fig. 3.7b. We can see that most of the error is due to imperfect rotation of the qubit, caused by ZZ error at low drive strengths. At high drive strengths, other errors also start to increase.

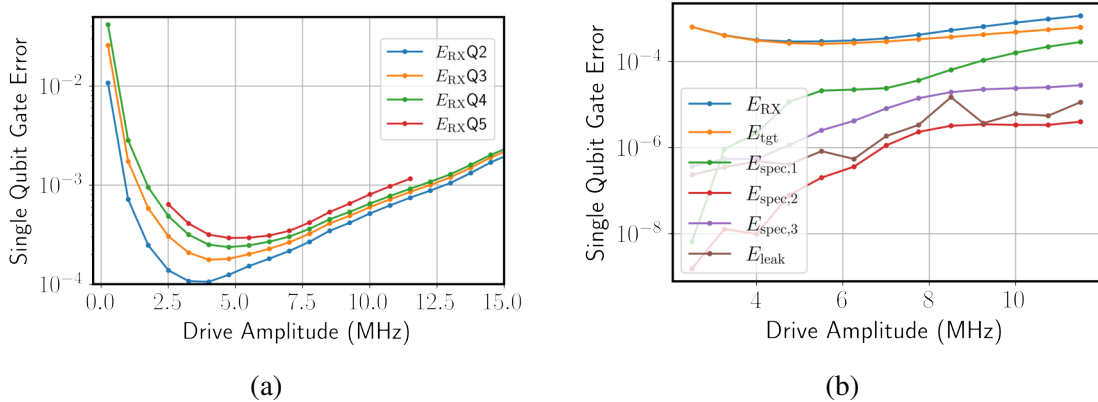


Figure 3.7: A study of the change in single qubit gate error with drive strength, as the system size changes. Qubit 5 is the driven qubit, and the spectators are added as shown in Fig. 3.6a. (a) shows the change in error with system size (Q2 represents 2 qubits and so on). (b) shows the error budget in a 5 qubit system.

Our analysis has helped us conclude that our choice of qubit frequencies given in Fig.

3.3a is a valid choice. We have also found various regions of operation around these frequencies where the gates will still have high fidelity. In the next chapter, we will consider the physical realization of this processor in a ring-resonator architecture (Hazra *et al.* (2021)).

CHAPTER 4

QUBIT DESIGN IN A 7 QUBIT RING-RESONATOR BASED PROCESSOR

In the previous chapter, we converged on a set of frequencies for the seven qubits in the processor. In this chapter, we will be discussing the physical implementation of this processor. In any quantum computer, qubit coherence and gate fidelity are some of the main considerations. Besides this, the connectivity of the processor also plays a role in reducing the number of gate operations required to implement an arbitrary gate/unitary operation.

Recently, a ring-resonator-based architecture was developed for increasing qubit connectivity (Hazra *et al.* (2021)). This allows us to create qubit networks with long-range, uniform inter-qubit coupling, which will greatly reduce the circuit depth of many operations. However, as discussed in Sec. 3.1, we know that dense connectivity causes increased static ZZ errors and a higher likelihood of frequency collisions.

One way in which this problem can be circumvented is by using tunable couplers, which create coupling between the qubits and the ring on demand. This can eliminate most of the coherent errors caused by coupling which is permanently on, since we can switch on the coupling between two qubits only when we need to implement a two-qubit gate between them.

However, for creating the first generation of processors based on this architecture, we have settled on a double ring resonator architecture as shown in Fig. 4.1a. The ring resonator offers a coupling that varies with the angle between the qubits placed on the ring. It operates based on wave interference between the two paths connecting the two qubits. (Hazra *et al.* (2021)).

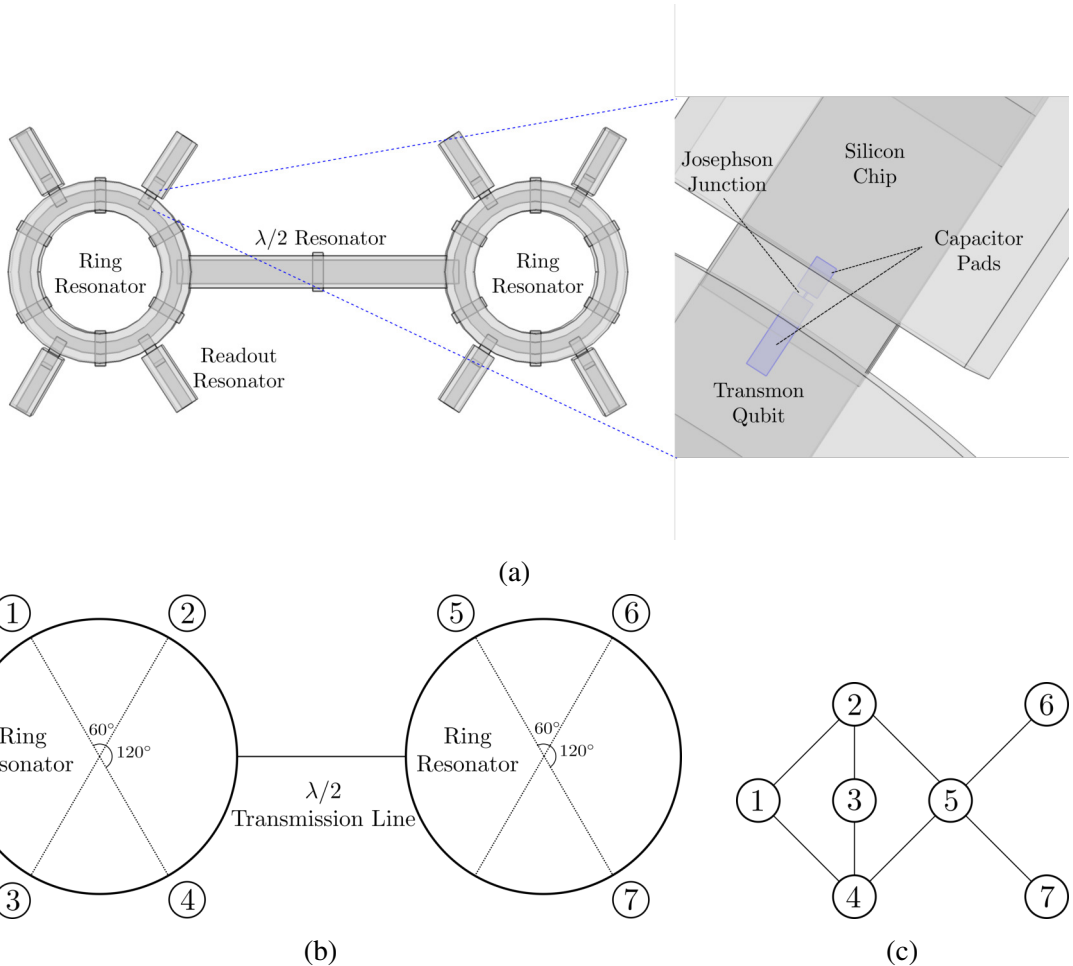


Figure 4.1: A schematic of the double-ring resonator structure. **(a)** A model of the double ring, with various elements labeled. The two ring resonators are connected by a $\lambda/2$ transmission line resonator with half the characteristic impedance of the ring resonator. Each slot in the ring resonator is spaced by angles shown in **(b)**. There are readout resonators connected to each slot to enable qubit readout and drive. **(b)** A schematic representation of where the qubits are placed in the double-ring and the angles between the various slots. **(c)** The connectivity that arises as a result of the placement shown in **(b)**

It can be shown that for qubits placed at angles of 60° and 180° within a ring, the inter-qubit exchange coupling is the same. For qubits placed at 120° , there is interferometric cancellation, and the qubits are not coupled. When two rings are connected by a $\lambda/2$ transmission line resonator with half the characteristic impedance of the ring resonator, the angles of the qubits relative to the resonator will obey the same rules. For example,

qubit 2 and qubit 5 (as shown in Fig. 4.1b) are effectively at an angle of 60° , causing them to be coupled. However, these rules apply only when the qubits are located in a small band of frequencies between the fundamental and first excited mode of the ring (Hazra *et al.* (2021)). In our situation, the fundamental mode is at 3.41 GHz, and the first excited mode is at 6.76 GHz. Thus, the qubit frequencies have to be located in a ≈ 300 MHz band around 5.08 GHz, which we call the special frequency of the ring resonator.

To obtain a processor with connectivity that is not too high (so as to minimize coherent errors) and to still have a significant number of connected qubits, we choose a placement of qubits as shown in Fig. 4.1b. Following the rules described above, the connectivity of the seven qubit system can be deduced, as shown in Fig. 4.1c. This is the same connectivity that we have analyzed in Chapter 3.

There are various electromagnetic quantities that determine the parameters of the qubit. The capacitance between the qubit pads (See Fig. 4.1a) determines the anharmonicity of the qubit. The electromagnetic interaction between two qubits, as given by the scattering matrix between the two junctions, determines their coupling. The interaction between the qubit and the readout cavity determines the rate at which qubit measurement can be implemented. The main determinant of such parameters is the dimensions of the qubit pads. The pads set up the capacitance across the Josephson junction in between them. The pads also determine the coupling between the qubit and the readout cavity and in between qubits. This is because the pads are capacitively coupled to the ring resonator and to the readout cavity. We perform finite element simulations on the double ring structure to extract estimates of all relevant quantities. We then iteratively converge on the dimensions of the qubit. These approaches are described in the sections below.

4.1 QUBIT CAPACITANCE

The simplest quantity to estimate is the qubit capacitance. We saw in Sec. 1.1.1 that the anharmonicity of a transmon qubit is given by $\alpha = -E_C/\hbar$, where $E_C = e^2/2C$, where e

is the charge of an electron and C is the capacitance across the junction. Thus, we need to estimate this quantity to get the right anharmonicity for each of our qubits.

The dimensions of the qubit pads and the distance between them are the main determinants of the qubit's capacitance. The surrounding metal structures also play a role. We compute the qubit by creating two terminals, one on each pad of the qubit, and set their potentials to 1V and 0V. We then allow the rest of the metal structure to have floating potentials. After this, we mesh the structure and compute the voltage distribution throughout the structure. This also gives us the charge on each of the qubit pads, and we can then determine the qubit capacitance. This is shown in Fig. 4.2.

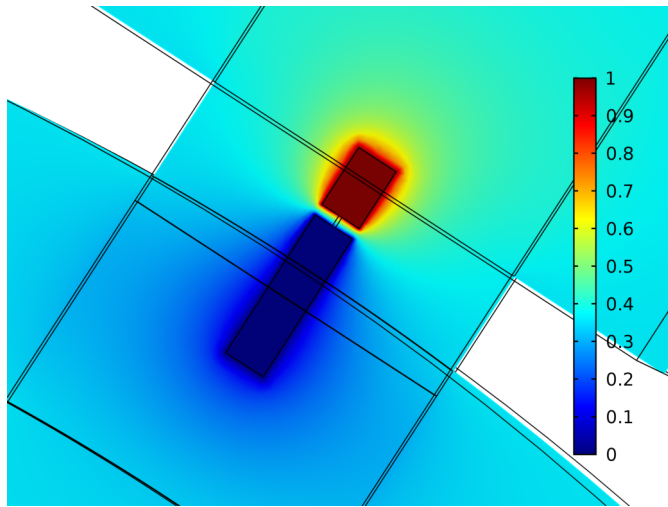


Figure 4.2: Distribution of electric potential in the plane of the qubit. The terminals are the pads of the qubit, set at 1V and 0V. The metal structures are defined as floating potentials in the electrostatic simulation.

4.2 READOUT COUPLING

In most transmon qubit architectures, the conventional way of driving and reading out the qubit is by coupling the qubit to a cavity/resonator. The cavity is then coupled to the microwave drive lines. The cavity's frequency (ω_C) and qubit's frequency (ω_Q) are chosen to be far apart as compared to the rate of exchange of photons between them ($\Delta = \omega_C - \omega_Q \gg g$), which is called the dispersive coupling regime. The interaction between the qubit and cavity is modeled by the Jaynes-Cummings Hamiltonian in the

dispersive limit:

$$\hat{H} = \frac{1}{2}\hbar\omega_Q\hat{\sigma}_Z + \hbar\omega_C(\hat{a}^\dagger\hat{a} + \frac{1}{2}) + \hbar\chi\hat{\sigma}_Z(\hat{a}^\dagger\hat{a} + \frac{1}{2}) \quad (4.1)$$

The first two terms are the Hamiltonians of the qubit and the cavity, and the third term is the dispersive shift term, where $\chi = g^2/\Delta$ is the dispersive shift. Due to this, the frequency of the cavity is dependent on the state of the qubit. Driving the cavity at its frequency will result in a phase shift in the scattered signal. This can be used to perform qubit measurement, and this process is called dispersive readout. Our goal is to determine the parameter g since it determines the magnitude of the cavity shift (Blais *et al.* (2004)).

The readout cavity is generally driven by inserting a pin connected to a coaxial cable/connector into it. This couples the cavity to the environment, causing a particular decay rate of photons in the cavity. When we couple the qubit to the cavity, the qubit's excitations can also decay via this process. This is called the Purcell effect (Purcell *et al.* (1946)). However, when the qubit is far detuned from the cavity, this effect is minimized. When the qubit is brought into resonance with the cavity, this effect is greatly enhanced. When near resonance, the rate of decay of the qubit's excitation (T_1) is given by the Purcell formula:

$$T_1 = \frac{1}{\kappa} \left(\frac{\Delta}{g} \right)^2 \quad (4.2)$$

Here, κ is the linewidth of the readout cavity, g is the coupling between the qubit and the cavity, and Δ is the detuning between the qubit and the cavity. It is simple to determine the linewidth of the cavity. We sweep the drive frequency on the cavity near resonance and compute the scattering parameters from the drive port. We then fit a Lorentzian through the reflection amplitude from this port and extract the linewidth and resonant frequency, as shown in Fig. 4.3b.

Now, we need to estimate the Purcell T1 of the qubit. It can be shown that the admittance seen by a port placed at the junction of the qubit pads ($Y(\omega_Q)$) gives us the Purcell T1

(Reed *et al.* (2010)):

$$T_1(\omega_Q) = \frac{C_Q}{Re(Y(\omega_Q))} \quad (4.3)$$

Here, C_Q is the capacitance of the qubit, which we have determined using electrostatic simulations. We then vary the frequency of the qubit (ω_Q) and compute the Purcell T_1 by using finite element simulations to find the admittance seen at the port located at the qubit junction (See Fig. 4.3a). While performing this simulation, the readout port is terminated with a 50 Ohm impedance, which is the environment seen at the readout pin. A parabola is fit through these points, as shown in Fig. 4.3c. Now, using Eq. 4.2, we get the coupling g , since we have already estimated the linewidth κ .

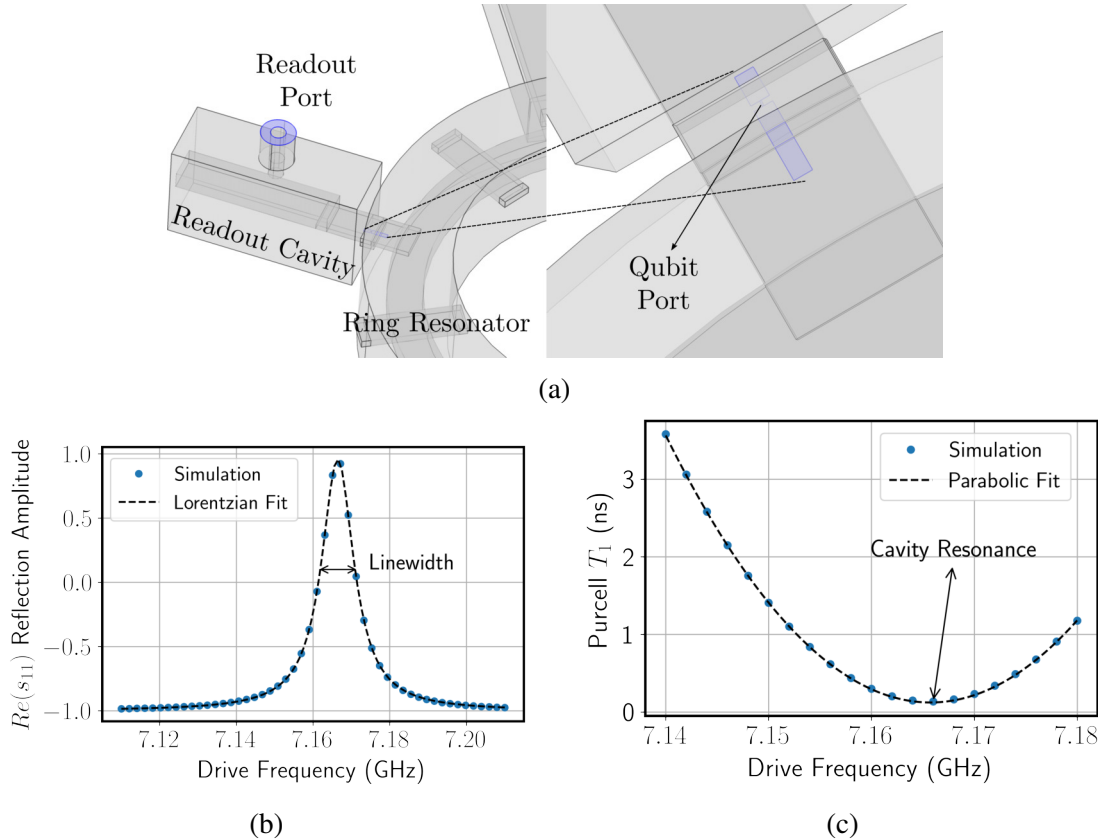


Figure 4.3: Estimating the cavity qubit coupling. **(a)** A schematic of the ports in the system. The readout port is driven, and the scattering matrix is estimated at this port to determine the cavity linewidth as shown in **(b)**. Subsequently, the readout port is terminated with a 50 Ohm impedance to model the environment, and then the qubit port is driven to determine the impedance seen from the qubit port. This is used to generate the Purcell fit in **(c)**

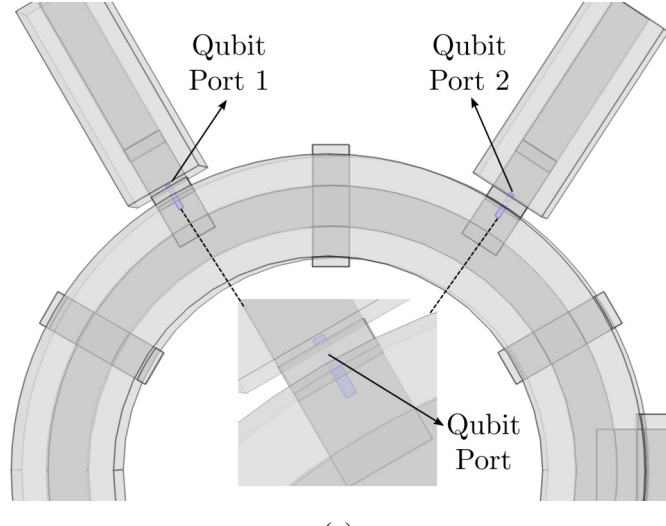
4.3 INTER QUBIT COUPLING

One of the most important parameters that needs to be verified in this structure is the inter-qubit coupling strengths for different pairs of qubits. For example, although the ring resonator architecture cancels inter qubit coupling for qubits located at an angle of 120° , due to a minor length mismatch, this might not be the case. To get an accurate idea of the coupling between various qubits, we use finite element simulation to extract estimates.

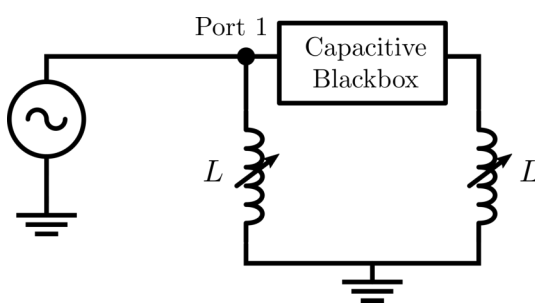
To extract the inter-qubit coupling between two qubits, we consider a two-port network as shown in Fig. 4.4a. We place two ports in two qubits and compute the scattering matrix between these two ports. Given that we do not have any inductive elements in the qubit that is simulated (the Josephson junction is not considered in the simulation), we get only the capacitive components of this two-port network.

We use the scattering matrix to create a black-box element, which contains the electromagnetic description of the ring resonator connecting the two qubits. We then consider two inductors at each port of this two-port black-box. (See Fig. 4.4b). The inductors are tuned to create two identical oscillators. This is equivalent to bringing the two qubits on resonance. This causes an avoided crossing/splitting of the peaks, which we can see in the scattering parameters of this two-port circuit. The coupling strength is given by half the value of the splitting between the two resonances. If the splitting is 6.6 MHz for a particular pair of qubits, their exchange coupling is then 3.3 MHz.

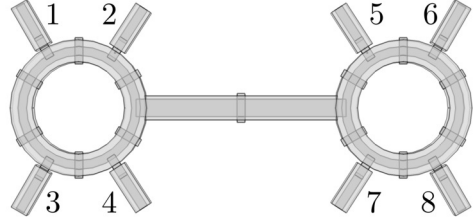
In a double ring structure, there are various qubit-qubit pairs possible. However, due to symmetries in the system, we only need to simulate a smaller subset of the qubits. These subsets are listed in the caption of Fig. 4.4c. For each such pair, the scattering matrix is extracted, and an avoided crossing experiment is performed as described above. This simulation is done over a range of frequencies around the special point of the ring resonator (5.08 GHz). All these plots are shown in Fig. 4.4d. The coupling strengths for the various pairs is summarized in Fig. 4.4e.



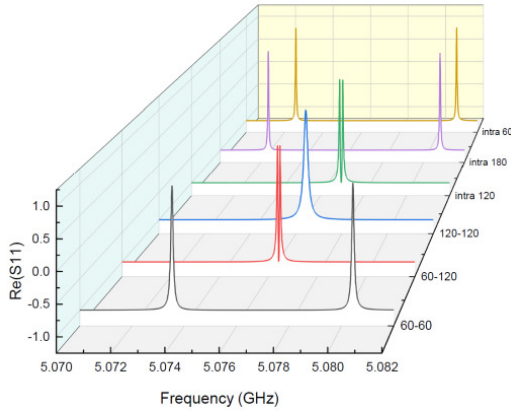
(a)



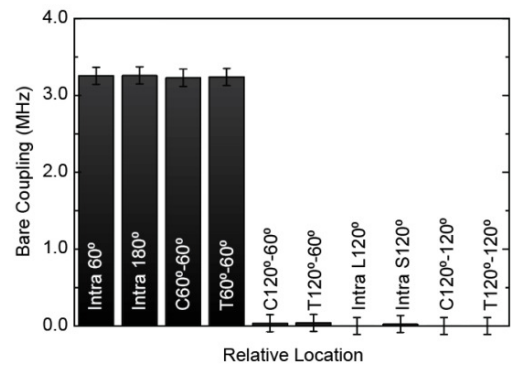
(b)



(c)



(d)



(e)

Figure 4.4: (a) The two port simulation that is required to estimate inter qubit coupling. Port 1 and 2 are excited one by one. Each port is located at the Josephson junction between the qubit pads. (b) Schematic circuit to observe an avoided crossing, as shown in (d). The blackbox element is extracted from finite element simulation (c) Cis-Trans naming convention: 1, 2 - Intra 60° . 1, 4 - Intra 180° . 1, 3 - Intra $L120^\circ$. 2, 4 - Intra $S120^\circ$. 2, 5 - Cis(C) $60^\circ - 60^\circ$. 2, 7 - Trans(T) $60^\circ - 60^\circ$. 2, 6 - $C60^\circ - 120^\circ$. 2, 8 - $T60^\circ - 120^\circ$. 3, 6 - $C120^\circ - 120^\circ$. 3, 8 - $T120^\circ - 120^\circ$. (d) Plots of avoided crossings. The coupling strength is half of the splitting. (e) A measure of the bare coupling extracted from the avoided crossing experiment.

We have thus fully characterized the most important parameters in the seven-qubit system. This design is then iteratively refined by comparison with experiment. We have to note that there is usually some mismatch between experiment and the estimates obtained from finite element simulation. However, this gives us a starting point to help us converge faster toward the final design.

CHAPTER 5

CONCLUSIONS AND FUTURE WORK

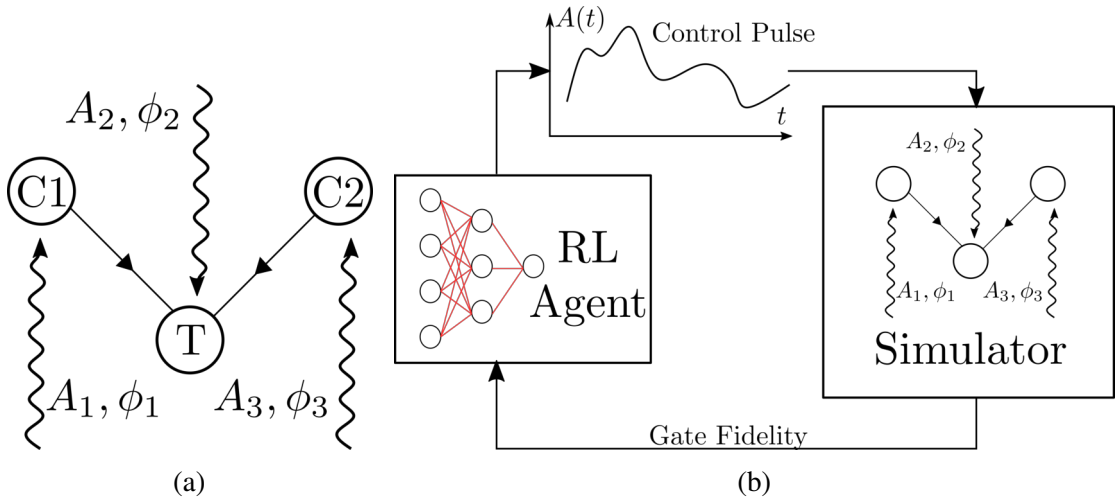
We have thus developed a framework to analyze cross resonance gates in a superconducting processor created from fixed-frequency transmon qubits. This was applied to a seven-qubit processor to help find frequencies for the qubits and to estimate tolerances on these values. Besides this, we have also explored the design of transmon qubits in a 3D circuit quantum electrodynamics architecture, using finite element electromagnetic simulations.

We now discuss various directions of research that emerge from the conclusions we have arrived at. Since the bulk of the work in this thesis was related to numerical simulations of superconducting qubits, we shall look at applying these techniques to other scenarios. We shall also look at other methods to analyze the performance of such processors.

5.1 ENHANCING THE GATE SET

We have studied the CR gate as the main entangling gate in all our connected qubit networks. However, recent studies have come up with other gates which are suitable for fixed frequency qubit architectures. One example is that of the iToffoli gate (Kim *et al.* (2022)). This 3-qubit gate can be implemented between any three qubits that are connected in a linear chain, as shown in Fig. 5.1a. Here, the two target qubits and the control qubit are driven at the frequency of the target ω_T . These create two cross resonance interactions between each control qubit and the target qubit. The drive on the target qubit also creates a single qubit rotation. The amplitudes and phases of these drives can be tuned to implement a Toffoli gate. This is an example of a multi-qubit operation implemented using two-qubit interactions. Since this is based on the cross resonance effect, we can apply all the tools developed to analyze this gate and extract its fidelity, and find operating points.

There are also other gates like the controlled phase gate (Krinner *et al.* (2020)) and the siZZle gate (Wei *et al.* (2021)), which can be implemented in fixed frequency architectures. The C-phase gate involves creating an interaction between the $|2\rangle|0\rangle$ and the $|0\rangle|1\rangle$ states of two qubits. This is done by inducing a Raman transition between these states by the use of a single microwave drive. The siZZle gate is also an all-microwave gate, which is implemented by off-resonantly driving qubits to create ZZ rotations, which can then be tuned to achieve a CZ gate. All these gates are applicable to our processor and can be analyzed by using the tools built, by modifying the unitary to which we compare our propagator.



5.2 OPTIMAL CONTROL TECHNIQUES

In Chapter 2, we saw that our pulse shape for driving the CR gate was just a simple cosine rise, flat-top pulse (see Fig. 2.5). Recent studies have found much better pulse shapes that increase gate fidelity and reduce gate time (Kirchhoff *et al.* (2018); Sivak

et al. (2022); Baum *et al.* (2021)). All these approaches are based on using a machine learning technique or a reinforcement learning (RL) agent to learn pulse shapes which offer better fidelity.

In Fig. 5.1b, we show a schematic of how this approach can be applied to the simulator that we have built. The simulator essentially uses the tools described in this thesis to compute gate fidelity. The RL agent learns the optimal control pulse by iteratively minimizing gate error. This is done by interacting with the simulator by supplying the control pulse to the simulator and using the gate fidelity it returns as a reward for converging on near-optimal pulse shapes.

5.3 PROCESSOR DIAGNOSTICS: EFFECTIVE HAMILTONIAN ESTIMATION AND STABILITY

In Sec. 2.2, we saw the effective Hamiltonian of two qubits interacting via the cross resonance effect. The terms in this expansion tell us the relative strengths of the useful terms (ω_{ZX}, ω_{IX}) as opposed to coherent error terms (ω_{ZZ}, ω_{IZ}). In a recent study of the cross resonance gate (Malekakhlagh *et al.* (2020)), this approach was extended to 3 qubit systems. This approach is based on the time-dependent Schrieffer-Wolff perturbation theory. A possible line of research would be to extend these methods to multi-qubit networks and compute the effective Hamiltonian.

In another recent study of the transmon platform for quantum computing (Berke *et al.* (2020)), various other metrics for analyzing a processor were developed. This study investigated the stability of the many-body localized (MBL) phase in coupled qubit networks. The stability of this parameter determines the extent to which individual qubit states are protected and localized. The intuition behind this is the fact that densely connected qubit networks have more and more level collisions, resulting in a chaotic spectrum, which adversely affects our ability to control these systems accurately. The tools developed in this study, like the statistics of many-body wave functions, Walsh

transforms and Kullback-Leibler analysis of spectral statistics can be applied to our 7-qubit processor to test our design choices.

5.4 MIXED INTEGER PROGRAMMING TO OPTIMIZE QUBIT FREQUENCIES

Given that fixing frequencies for just seven qubits is tedious, we tried to develop an automated optimization function to choose the frequencies of all qubits. This was based on the idea of creating an optimizer to maximize the distance of the seven frequency choices from all the poles listed in Sec. 2.2. We formulate this optimization problem in terms of the detuning values x_i in the processor, which are our continuous variables. In Sec. 2.2, we saw that the CR gate divides the control-target detuning landscape into multiple regions (See Fig. 2.5) The choices for the regions in the frequency landscape are represented by integers r_i in our formulation (See Fig. 5.2). We note that only two regions $0 < \Delta_{ct} < -\alpha/2$, $-\alpha/2 < \Delta_{ct} < -\alpha$ are favourable for the cross resonance gate (See Sec. 2.2). Thus, the numbers r_i take only values 1, 2. We define an objective function as follows:

$$O = \sum_i |x_i| + \delta(r_i, 1)|x_i - (-\alpha/2)| + \delta(r_i, 2)|x_i - (-\alpha)| + \left(\sum_{j \in \text{shared control}} |x_i - x_j| + |x_i - x_j + \alpha| \right) \quad (5.1)$$

where $\delta(r_i, n) = 1$ if $r_i = n$ and 0 otherwise. Maximizing this objective function will ensure that each of the detuning values x_i are chosen so that the distance from the poles is maximized.

Optimizing this objective function with MIP solvers did not work directly since many x_i were driven to zero. We did not come up with a method to circumvent this issue since we had already converged upon a list of candidate frequencies. However, very recently, Morvan *et al.* Morvan *et al.* (2021) used a very similar approach and modified

the objective function to converge on non-trivial solutions. This approach can be adopted to verify and improve our frequency choices.

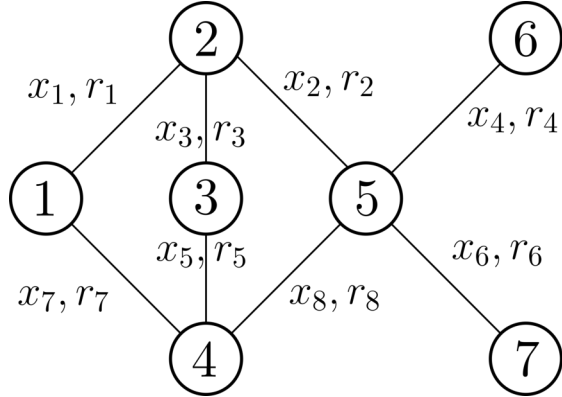


Figure 5.2: The set of variables for mixed integer programming. Each directed edge is associated with a continuous variable x_i and an integer r_i depicting which region in the frequency landscape (Refer Fig. 2.3) the detuning x_i belongs to.

5.5 CONCLUSION

The main line of research in this thesis was to develop tools to analyze and optimize connected qubit networks in which the cross resonance gate is the native two-qubit gate. This was done by creating a formalism that defines families of unitary matrices and extracting such matrices from the unitary propagator of the system. These tools were applied to connected qubit networks, and specifically to design a seven-qubit processor. Various design choices were validated using this approach.

We also discussed the use of finite element simulations to design qubits in the seven-qubit processor. This was done in the context of the double ring-resonator setup. Finally, we discussed various extensions of the work done in this thesis. We hope this set of tools and approaches will motivate further analysis and will prove to be useful in the design of better and more accurate quantum computers.

APPENDIX A

MATHEMATICAL METHODS

In this chapter, we detail the mathematical methods used in our simulations. This describes the details of how we find the unitary matrices belonging to the various families described in Sec. 2.3.3, 2.4, and concludes with a description of other software packages and numerical methods used.

A.1 METHODS: ESTIMATING THE CLOSEST UNITARY

A.1.1 Two Qubit Analysis

For a system of 2 qubits consisting of a control and target, the ideal CR gate unitary matrix belongs to the family \mathcal{U}_{CR} , as specified in Eq. 2.7. To understand how to find $U_{\text{CR}} \in \mathcal{U}_{\text{CR}}$ so that F_{MU} is maximized, we need to consider the matrix form of the family \mathcal{U}_{CR} :

$$\mathcal{U}_{\text{CR}} = \begin{pmatrix} e^{i\theta_0} \cos \phi_0/2 & -ie^{i\theta_0} \sin \phi_0/2 & 0 & 0 \\ -ie^{i\theta_0} \sin \phi_0/2 & e^{i\theta_0} \cos \phi_0/2 & 0 & 0 \\ 0 & 0 & e^{i\theta_1} \cos \phi_1/2 & -ie^{i\theta_1} \sin \phi_1/2 \\ 0 & 0 & -ie^{i\theta_1} \sin \phi_1/2 & e^{i\theta_1} \cos \phi_1/2 \end{pmatrix} \quad (\text{A.1})$$

Comparing this form (Eq. A.1) with matrix M , we can derive expressions for $\theta_0, \theta_1, \phi_0, \phi_1$ as:

$$\phi_0 = -\text{angle} \left(\frac{M_{00} + M_{11} + M_{01} + M_{10}}{M_{00} + M_{11} - M_{01} - M_{10}} \right) \quad (\text{A.2})$$

$$\phi_1 = -\text{angle} \left(\frac{M_{22} + M_{33} + M_{23} + M_{32}}{M_{22} + M_{33} - M_{23} - M_{32}} \right) \quad (\text{A.3})$$

$$\theta_0 = \text{angle}[(M_{00} + M_{11}) \cos \phi_0/2 + i(M_{01} + M_{10}) \sin \phi_0/2] \quad (\text{A.4})$$

$$\theta_1 = \text{angle}[(M_{22} + M_{33}) \cos \phi_1/2 + i(M_{23} + M_{32}) \sin \phi_1/2] \quad (\text{A.5})$$

We can use these expressions to compute U_{CR} , which is then used to find gate fidelity as described in Sec. 2.3.3

A.1.2 Multiqubit Computation

In Sec. 2.4, we constructed the CR unitary matrix family and the families of matrices where qubits are sequentially allowed to rotate arbitrarily (Eq. 2.21, 2.22), for an arbitrary number of qubits. We need to find matrices $U_{\text{CR}} \in \mathcal{U}_{\text{CR}}, U^n \in \mathcal{U}^n$ belonging to these families which are closest to our propagator M . In the case of 2 qubits, we had simple analytical expressions (Eq. A.2). In the case of multiple qubits, we have constructed the following methods of extracting relevant parameters.

Consider the matrix form of Eq. 2.21. It will be block diagonal with blocks of 4×4 matrices of the form of the CR 2 qubit unitary (Eq. A.1):

$$U = \begin{pmatrix} CR_1 & 0 & \dots \\ 0 & CR_2 & \dots \\ \vdots & \ddots & \vdots \\ 0 & 0 & CR_{2^{N-2}} \end{pmatrix} \quad (\text{A.6})$$

where:

$$CR_i = \begin{pmatrix} e^{i\beta_i^0} \cos \phi_0/2 & -e^{i\beta_i^0} \sin \phi_0/2 & 0 & 0 \\ -e^{i\beta_i^0} \sin \phi_0/2 & e^{i\beta_i^0} \cos \phi_0/2 & 0 & 0 \\ 0 & 0 & e^{i\beta_i^1} \cos \phi_1/2 & -e^{i\beta_i^1} \sin \phi_1/2 \\ 0 & 0 & -e^{i\beta_i^1} \sin \phi_1/2 & e^{i\beta_i^1} \cos \phi_1/2 \end{pmatrix} \quad (\text{A.7})$$

Comparing Eq. A.6 and Eq. 2.21, we get

$$\beta_i^0 = \sum_{j=1}^{N-2} \theta_j b_j \quad (\text{A.8})$$

$$\beta_i^1 = \theta_c^1 + \sum_{j=1}^{N-2} \theta_j b_j \quad (\text{A.9})$$

where b_j represents the j^{th} bit of the $(N - 2)$ bit binary representation of the index i . This is because for the i^{th} element of the block diagonal, the tensor order given in Eq. 2.20 determines the qubits which are in state $|1\rangle$ by the binary expansion of the index.

With this understanding, we can divide the matrix M into 4×4 blocks (denoted by CR^M) of the form Eq. A.6, and extract:

$$\phi_i^0 = -\text{angle}\left(\frac{CR_{i,00}^M + CR_{i,11}^M + CR_{i,01}^M + CR_{i,10}^M}{CR_{i,00}^M + CR_{i,11}^M - CR_{i,01}^M - CR_{i,10}^M}\right) \quad (\text{A.10})$$

$$\phi_i^1 = -\text{angle}\left(\frac{CR_{i,22}^M + CR_{i,33}^M + CR_{i,23}^M + CR_{i,32}^M}{CR_{i,22}^M + CR_{i,33}^M - CR_{i,23}^M - CR_{i,32}^M}\right) \quad (\text{A.11})$$

$$\beta_i^0 = \text{angle}[(CR_{i,00}^M + CR_{i,11}^M) \cos \phi_i^0/2 + i(CR_{i,01}^M + CR_{i,10}^M) \sin \phi_i^0/2] \quad (\text{A.12})$$

$$\beta_i^1 = \text{angle}[(CR_{i,22}^M + CR_{i,33}^M) \cos \phi_i^1/2 + i(CR_{i,23}^M + CR_{i,32}^M) \sin \phi_i^1/2] \quad (\text{A.13})$$

$$i \in \{1, 2, \dots, 2^{N-2}\} \quad (\text{A.14})$$

Thus, we have an array of $2^{(N-2)}$ values for ϕ^0 and ϕ^1 . We take the average of these values to construct the closest unitary to M . If these values vary, it means that the rotation of the target qubit is conditioned on the state of the spectator qubits, which will indicate that the gate fidelity is low.

Constructing the set of $\theta_i \quad i \in \{1, 2, \dots, (N - 2)\}$, θ_c is not as simple as taking the average of these numbers. There are 2^{N-1} linear equations (Eq. A.12, A.13) with the RHS being β_i^0, β_i^1 with the LHS consisting of $(N - 1)$ variables θ_i, θ_c . Since this is an overspecified system of equations, we used the first $(N - 1)$ equations which involve all $(N - 1)$ variables. This is might not be the best choice. This system of equations is solved by using a least square solver available in NumPy, to yield initial values of θ_i, θ_c .

Our goal is to maximize $F_{M,U}$. This is a function of the parameters $\phi_0, \phi_1, \theta_i, \theta_c$. We thus use an optimizer from SciPy, which searches for optimal solutions based on

the Nelder-Mead search method. We maximize the function $F_{M,U}(\phi_0, \phi_1, \theta_i, \theta_c)$. We observed that the optimizer does not perform well if we do not give it a good starting point. Thus, the angles estimated from least square estimation are used as a starting point. The values that the optimizer converges to will then yield the closest unitary U from the family \mathcal{U}_{CR} as per Eq. 2.21. Constructing a matrix U^n from the family \mathcal{U}^n is also done in a similar fashion by extracting the closest unitary to each of the elements of the block diagonal, as described in Eq. 2.22. This is done using the SVD as detailed in Sec 2.3.3.

A.2 COMPUTATIONAL METHODS USED

We used the QuTiP (Johansson *et al.* (2013)) package to construct the Hamiltonian, perform time evolution and extract the Unitary propagator. To compare results and check accuracies, we also developed a Schrödinger equation solver based on the Magnus Expansion Blanes *et al.* (2009). Both solvers gave identical results, with the Magnus Expansion converging (with respect to discretization in time) more rapidly than the QuTiP solver, but needing more solution time. All this functionality to model the multiqubit system has been wrapped into a Python library. As discussed earlier, we use NumPy and SciPy to do all matrix computations and unitary matrix construction. We use COMSOL Multiphysics to perform all finite element simulations discussed in Chapter 4.

REFERENCES

1. **Baum, Y., M. Amico, S. Howell, M. Hush, M. Liuzzi, P. Mundada, T. Merkh, A. R. Carvalho, and M. J. Biercuk** (2021). Experimental deep reinforcement learning for error-robust gate-set design on a superconducting quantum computer. *PRX Quantum*, **2**, 040324. URL <https://link.aps.org/doi/10.1103/PRXQuantum.2.040324>.
2. **Berke, C., E. Varvelis, S. Trebst, A. Altland, and D. P. DiVincenzo** (2020). Transmon platform for quantum computing challenged by chaotic fluctuations.
3. **Blais, A., R.-S. Huang, A. Wallraff, S. M. Girvin, and R. J. Schoelkopf** (2004). Cavity quantum electrodynamics for superconducting electrical circuits: An architecture for quantum computation. *Phys. Rev. A*, **69**, 062320. URL <https://link.aps.org/doi/10.1103/PhysRevA.69.062320>.
4. **Blanes, S., F. Casas, J. Oteo, and J. Ros** (2009). The magnus expansion and some of its applications. *Physics Reports*, **470**(5), 151–238. ISSN 0370-1573. URL <https://www.sciencedirect.com/science/article/pii/S0370157308004092>.
5. **Brink, M., J. M. Chow, J. Hertzberg, E. Magesan, and S. Rosenblatt**, Device challenges for near term superconducting quantum processors: frequency collisions. In *2018 IEEE International Electron Devices Meeting (IEDM)*. 2018.
6. **Brown, K. L., W. J. Munro, and V. M. Kendon** (2010). Using quantum computers for quantum simulation. *Entropy*, **12**(11), 2268–2307. URL <https://doi.org/10.3390/entropy-12-2268>.
7. **Chamberland, C., G. Zhu, T. J. Yoder, J. B. Hertzberg, and A. W. Cross** (2020). Topological and subsystem codes on low-degree graphs with flag qubits. *Physical Review X*, **10**(1). ISSN 2160-3308. URL <http://dx.doi.org/10.1103/PhysRevX.10.011022>.
8. **Childress, L. and R. Hanson** (2013). Diamond nv centers for quantum computing and quantum networks. *MRS Bulletin*, **38**(2), 134–138.
9. **Chow, J. M., A. D. Córcoles, J. M. Gambetta, C. Rigetti, B. R. Johnson, J. A. Smolin, J. R. Rozen, G. A. Keefe, M. B. Rothwell, M. B. Ketchen, and M. Steffen** (2011). Simple all-microwave entangling gate for fixed-frequency superconducting qubits. *Phys. Rev. Lett.*, **107**, 080502. URL <https://link.aps.org/doi/10.1103/PhysRevLett.107.080502>.
10. **Devoret, M. H. and J. M. Martinis** (2004). Implementing qubits with superconducting integrated circuits. *Quantum Information Processing*, **3**(1), 163–203. ISSN 1573-1332. URL <https://doi.org/10.1007/s11128-004-3101-5>.
11. **DiVincenzo, D. P.** (2000). The physical implementation of quantum computation. *Fortschritte der Physik*, **48**(9-11), 771–783. URL [https://doi.org/10.1002/\(SICI\)1521-397X\(200009\)48:9/11<771::AID-PROP771>3.0.CO;2-1](https://doi.org/10.1002/(SICI)1521-397X(200009)48:9/11<771::AID-PROP771>3.0.CO;2-1).

12. **Grover, L. K.** (1996). A fast quantum mechanical algorithm for database search. URL <https://arxiv.org/abs/quant-ph/9605043>.
13. **Hazra, S., A. Bhattacharjee, M. Chand, K. V. Salunkhe, S. Gopalakrishnan, M. P. Patankar, and R. Vijay** (2021). Ring-resonator-based coupling architecture for enhanced connectivity in a superconducting multiqubit network. *Phys. Rev. Applied*, **16**, 024018. URL <https://link.aps.org/doi/10.1103/PhysRevApplied.16.024018>.
14. **Johansson, J., P. Nation, and F. Nori** (2013). Qutip 2: A python framework for the dynamics of open quantum systems. *Computer Physics Communications*, **184**(4), 1234–1240. ISSN 0010-4655. URL <https://www.sciencedirect.com/science/article/pii/S0010465512003955>.
15. **Kim, Y., A. Morvan, L. B. Nguyen, R. K. Naik, C. Jünger, L. Chen, J. M. Kreikebaum, D. I. Santiago, and I. Siddiqi** (2022). High-fidelity three-qubit iToffoli gate for fixed-frequency superconducting qubits. *Nature Physics*. URL
16. **Kirchhoff, S., T. Keßler, P. J. Liebermann, E. Assé mat, S. Machnes, F. Motzoi, and F. K. Wilhelm** (2018). Optimized cross-resonance gate for coupled transmon systems. *Physical Review A*, **97**(4). URL
17. **Koch, J., T. M. Yu, J. Gambetta, A. A. Houck, D. I. Schuster, J. Majer, A. Blais, M. H. Devoret, S. M. Girvin, and R. J. Schoelkopf** (2007). Charge-insensitive qubit design derived from the cooper pair box. *Phys. Rev. A*, **76**, 042319. URL <https://link.aps.org/doi/10.1103/PhysRevA.76.042319>.
18. **Krantz, P., M. Kjaergaard, F. Yan, T. P. Orlando, S. Gustavsson, and W. D. Oliver** (2019). A quantum engineer's guide to superconducting qubits. *Applied Physics Reviews*, **6**(2), 021318. URL
19. **Krinner, S., P. Kurpiers, B. Royer, P. Magnard, I. Tsitsilin, J.-C. Besse, A. Remm, A. Blais, and A. Wallraff** (2020). Demonstration of an all-microwave controlled-phase gate between far-detuned qubits. *Physical Review Applied*, **14**(4). URL
20. **Loss, D. and D. P. DiVincenzo** (1998). Quantum computation with quantum dots. *Phys. Rev. A*, **57**, 120–126. URL <https://link.aps.org/doi/10.1103/PhysRevA.57.120>.
21. **Magesan, E. and J. M. Gambetta** (2020). Effective hamiltonian models of the cross-resonance gate. *PHYSICAL REVIEW A*, **101**, 52308.
22. **Malekakhlagh, M., E. Magesan, and D. C. McKay** (2020). First-principles analysis of cross-resonance gate operation. *Physical Review A*, **102**, 42605.
23. **Morvan, A., L. Chen, J. M. Larson, D. I. Santiago, and I. Siddiqi** (2021). Optimizing frequency allocation for fixed-frequency superconducting quantum processors.

24. **Munro, W. J., G. J. Milburn, and B. C. Sanders** (2000). Entangled coherent-state qubits in an ion trap. *Phys. Rev. A*, **62**, 052108. URL <https://link.aps.org/doi/10.1103/PhysRevA.62.052108>.
25. **Pedersen, L. H., N. M. Møller, and K. Mølmer** (2007). Fidelity of quantum operations. *Physics Letters A*, **367**(1), 47–51. ISSN 0375-9601. URL <https://www.sciencedirect.com/science/article/pii/S0375960107003271>.
26. **Purcell, E. M., H. C. Torrey, and R. V. Pound** (1946). Resonance absorption by nuclear magnetic moments in a solid. *Phys. Rev.*, **69**, 37–38. URL <https://link.aps.org/doi/10.1103/PhysRev.69.37>.
27. **Reed, M. D., B. R. Johnson, A. A. Houck, L. DiCarlo, J. M. Chow, D. I. Schuster, L. Frunzio, and R. J. Schoelkopf** (2010). Fast reset and suppressing spontaneous emission of a superconducting qubit. *Applied Physics Letters*, **96**(20), 203110. URL
28. **Rigetti, C. and M. Devoret** (2010). Fully microwave-tunable universal gates in superconducting qubits with linear couplings and fixed transition frequencies. *Phys. Rev. B*, **81**, 134507. URL <https://link.aps.org/doi/10.1103/PhysRevB.81.134507>.
29. **Sheldon, S., E. Magesan, J. M. Chow, and J. M. Gambetta** (2016). Procedure for systematically tuning up cross-talk in the cross-resonance gate. *RAPID COMMUNICATIONS PHYSICAL REVIEW A*, **93**, 60302.
30. **Shor, P. W.** (1997). Polynomial-time algorithms for prime factorization and discrete logarithms on a quantum computer. *SIAM Journal on Computing*, **26**(5), 1484–1509. URL
31. **Sivak, V., A. Eickbusch, H. Liu, B. Royer, I. Tsoutsios, and M. Devoret** (2022). Model-free quantum control with reinforcement learning. *Physical Review X*, **12**(1). URL
32. **Tripathi, V., M. Khezri, and A. N. Korotkov** (2019). Operation and intrinsic error budget of a two-qubit cross-resonance gate. *Phys. Rev. A*, **100**, 012301. URL <https://link.aps.org/doi/10.1103/PhysRevA.100.012301>.
33. **Wei, K. X., E. Magesan, I. Lauer, S. Srinivasan, D. F. Bogorin, S. Carnevale, G. A. Keefe, Y. Kim, D. Klaus, W. Landers, N. Sundaresan, C. Wang, E. J. Zhang, M. Steffen, O. E. Dial, D. C. McKay, and A. Kandala** (2021). Quantum crosstalk cancellation for fast entangling gates and improved multi-qubit performance. URL <https://arxiv.org/abs/2106.00675>.
34. **Zanardi, P. and D. A. Lidar** (2004). Purity and state fidelity of quantum channels. *Phys. Rev. A*, **70**, 012315. URL <https://link.aps.org/doi/10.1103/PhysRevA.70.012315>.